Supporting Information for:

Crimping-induced structural gradients explain the lasting strength of poly L-lactide bioresorbable vascular scaffolds during hydrolysis

Karthik Ramachandran[a], Tiziana Di Luccio[a,b], Artemis Ailianou[a], Mary Beth Kossuth[c], James P. Oberhauser[c,1] & Julia A. Kornfield[a,2]

[a]Division of Chemistry and Chemical Engineering, California Institute of Technology, 1200 E California Blvd, Pasadena, CA 91125, USA

[b]Division of Sustainable Materials, ENEA, Centro Ricerche Portici, I-80055, Italy

[c]Global Product Development, Abbott Vascular, 3200 Lakeside Drive, Santa Clara, CA 95054, USA

[1]Present address: Gilead Sciences, Inc., Foster City, CA, 94404.

[2]To whom correspondence should be addressed: jakornfield@cheme.caltech.edu

Author Contribution

K.R. and J.A.K. designed research; K.R. and T.D.L performed research; A.A, M.B.K. and J.P.O contributed new reagents/analytic tools; K.R. and J.A.K. analyzed data; K.R. and J.A.K wrote the paper.

Conflict of Interest: Two of the authors (M.B.K and J.P.O) are employees of Abbott Vascular. Funding for this research was provided by Abbott Vascular.

Keywords: PLLA, Hydrolysis, Coronary Heart Disease, BVS, X-ray Microdiffraction

Classification: Physical Sciences, Applied Physical Sciences

Characterizing the molecular weight, mass and radial strength of hydrolyzed scaffolds

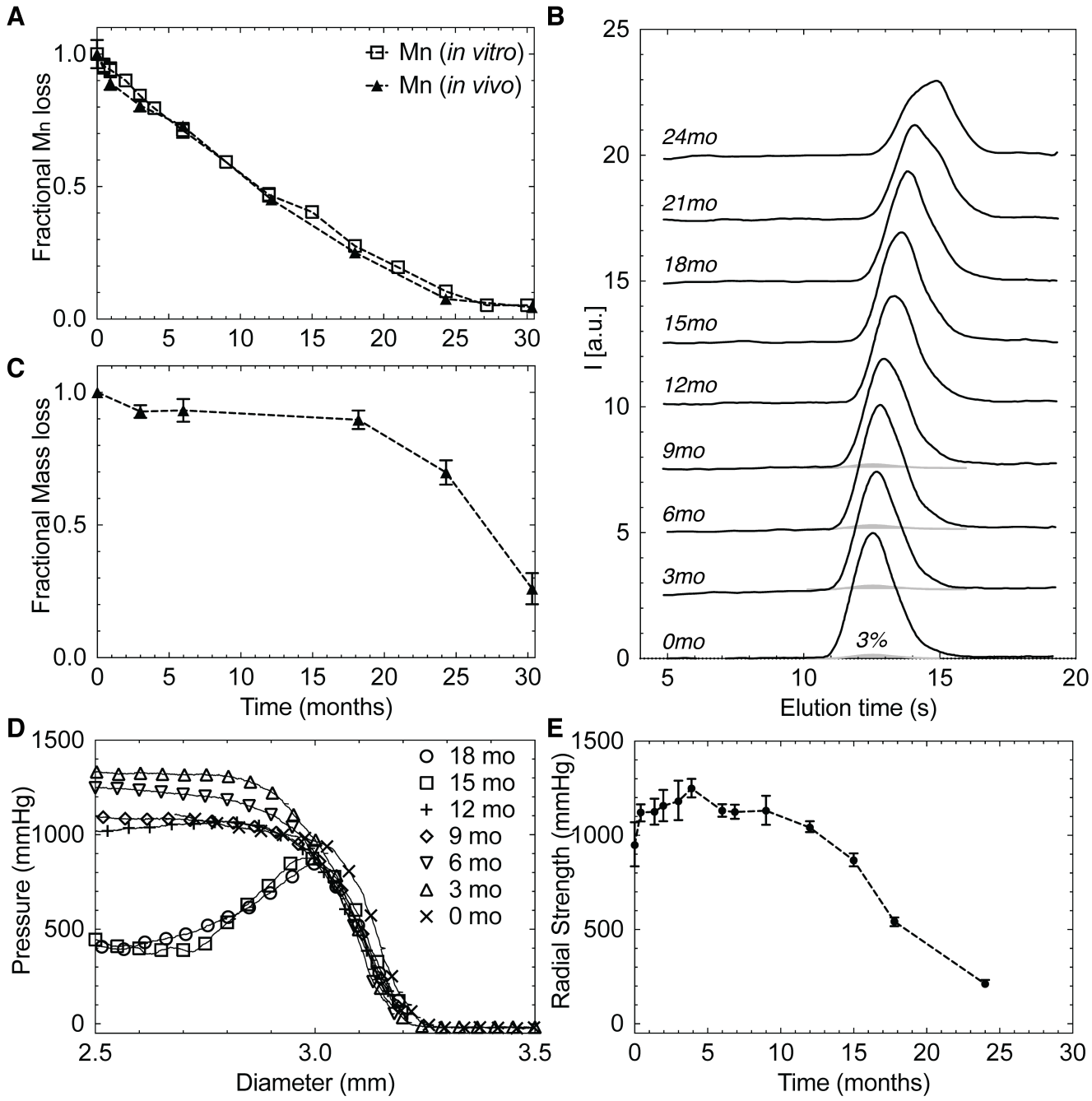

Fig. S1. Impact of hydrolysis (*A*) both *in vitro* (phosphate-buffered saline at 37°C) and *in vivo* (coronary artery of porcine model) on the normalized number average molecular weight (M_n) of BVSs. The gel-permeation chromatography (GPC) traces in (*B*) correspond to the fractional M_n values in (*A*). The traces labelled 3% (gray lines in *B*) indicate that longer chains in the hydrolysis-resistant regions, which make up <3% of the scaffold, are challenging to detect (GPC data are acquired by dissolving an entire scaffold). *In vitro* hydrolyzed scaffolds are further analyzed to determine (*C*) normalized mass loss, (*D*) pressure-diameter trace (acquired by subjecting BVSs to increasing compressive stress using an MSI RX550 radial force tester; a single representative curve out of a total of 6 is presented for clarity), and (*E*) radial strength ($n = 6$). Where error bars are not shown (*A*, *C* and *E*), the uncertainty is smaller than the symbol. The radial strength in (*E*) is computed from pressure diameter traces in (*D*)

by Abbott Vascular as per ASTM F3067 standards. For each measurement, a tangent line is drawn parallel to the part of the trace that displays a linear increase in pressure with decreasing diameter (similar in principle to estimating the modulus from stress-strain data). A second line, offset by 0.1 mm, is drawn parallel to the tangent line to account for plastic deformation of the scaffold due to arterial contractions. The maximum pressure bounded by the two tangent lines is then reported as the radial strength of the BVS. In addition to co-authors M.B.K. and J.P.O, the following Abbott Vascular employees contributed to these experiments: Susan Veldhof, Syed F.A. Hossainy and Richard Rapoza. Fig. S1*A*, *C* & *E* present data from Ref. (1) and Fig. S1*D* presents data from Ref. (2).

Polarized light micrographs of ~15µm sections cut from three different 18M scaffolds

Fig. S2. Polarized light micrographs of ~15μm thick sections cut from three different scaffolds hydrolyzed for 18M (*A-C*). The scaffolds were produced from the same batch of material using the same processing conditions. The sections presented in (*A*) were used for X-ray microdiffraction studies.

Polarized light micrographs of ~15µm sections cut from three different 9M scaffolds

Fig. S3. Polarized light micrographs of ~15μm thick sections cut from three different scaffolds hydrolyzed for 9M (*A-C*). The scaffolds were produced from the same batch of material using the same processing conditions. The sections presented in (*A*) were used for X-ray microdiffraction studies.

Polarized light micrographs of ~15µm sections cut from three different as-deployed scaffolds

Fig. S4. Polarized light micrographs of ~15μm thick sections cut from three different as-deployed (0M) scaffolds (*A-C*). The scaffolds were produced from the same batch of material using the same processing conditions. The sections presented in (*A*) were used for X-ray microdiffraction studies.

Quantitative characteristics of sections cut ~60µm from the ID of the 0M, 9M and 18M BVS

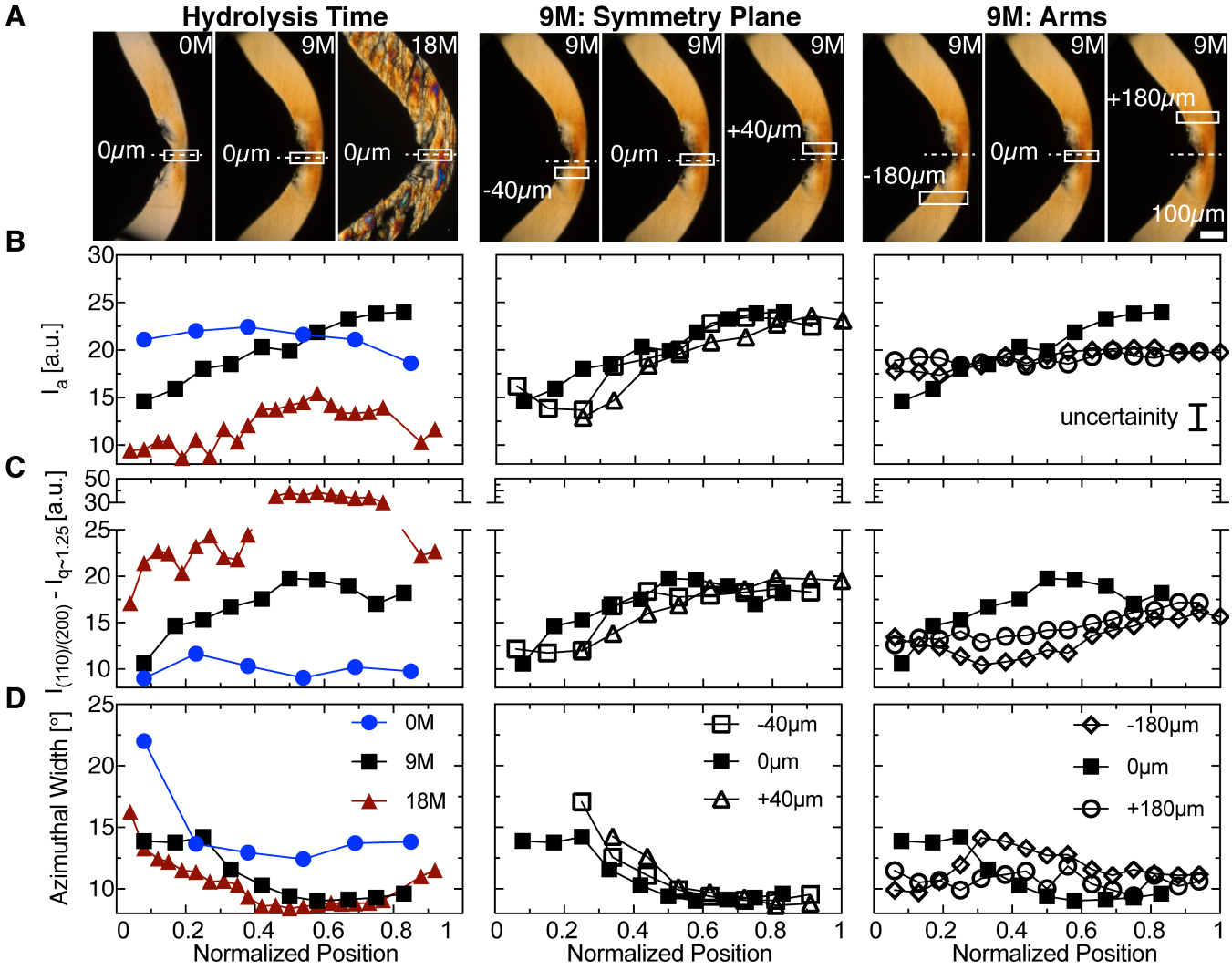

Fig. S5. Quantitative characteristics of microdiffraction data acquired along lines in white rectangles in (*A*) polarized light micrographs from sections taken ~60*µ*m from the ID of scaffolds subjected to 0M, 9M and 18M hydrolysis: (*B*) the intensity of the noncrystalline halo, I_a averaged over $q \in [0.95\text{-}1.05 Å^{-1}]$, (*C*) the intensity associated with crystalline diffraction, $I_{max,(110)/(200)} - I_{q\sim1.25}$ and (*D*) full-width at half maximum of the (110)/(200) peaks. In *B-D*, (*left*) effect of hydrolysis time at the symmetry plane; (*center*) effect of 40 *µ*m displacement from the symmetry plane; (*right*) effect of 180 *µ*m displacement from the symmetry plane. Uncertainty in the intensity due to variations in section thickness is indicated by the vertical bar in *B*, *right* determined as described in Fig. S6. Legends for *B* and *C* are shown in *D*. Normalized position varies from 0 at IB to 1 at OB.

Estimating the uncertainty in thickness of the ~15µm thick PLLA sections

The clinically-approved scaffolds (as-deployed and hydrolyzed) were microtomed from the outer to the inner diameter to yield ~15µm thick consecutive sections of a U-crest. To estimate the variation in thickness from one section to another, we probe the amorphous content along the arms of the U-crest as the arms experience little to no deformation during crimping or deployment. As a result, the amorphous content at the arms serves as an internal standard for the thickness of the section.

In contrast to the material near the symmetry plane, the material at the arms has a uniform morphology – there is hardly any variation in the amorphous content from the inner (IB) to the outer bend (OB) for four different sections cut from the same 9M scaffold (Fig. S6). However, subtle variations in amorphous content from one section to another suggest ~1µm variations in sample thickness.

We use the standard deviation in amorphous content (I_a = 18.72 ± 1.25 a.u.; calculated using all data presented in Fig. S6) to define an error bar for the calculations presented in Figure S5. We find that the variations in the sample thickness do not affect our interpretation of the gradients in amorphous content from the symmetry plane to the arms.

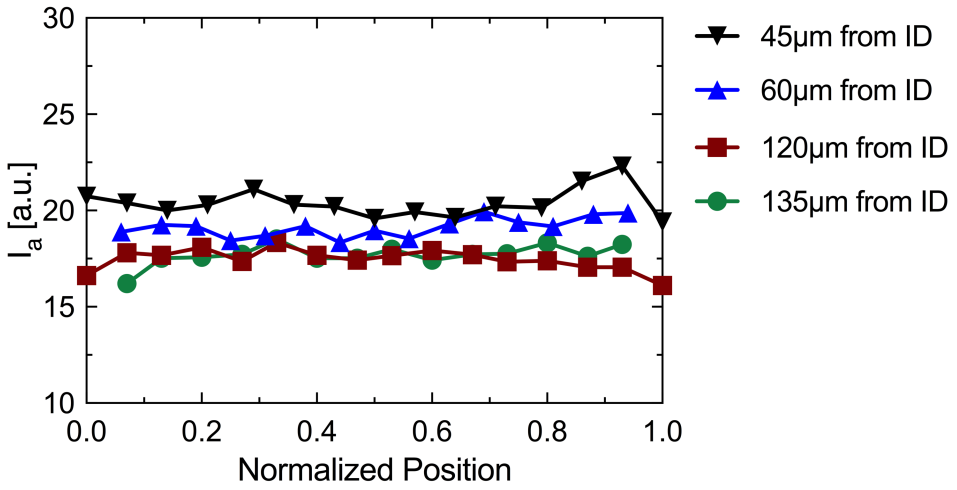

Fig. S6. The mean of the azimuthally averaged intensity, I(q), between $q \in [0.95 – 1.05]$ Å^{-1} is used as a measure of amorphous content (I_a) in each section. We present the variation in amorphous content from the inner (IB) to the outer bend (OB) along the arms of ~15μm thick sections cut 45μm, 60μm, 120μm and 135μm from the inner diameter of the 9M scaffold. Normalized position varies from 0 at the IB to 1 at OB.

Origin of high-retardance microdomains in 18M scaffolds

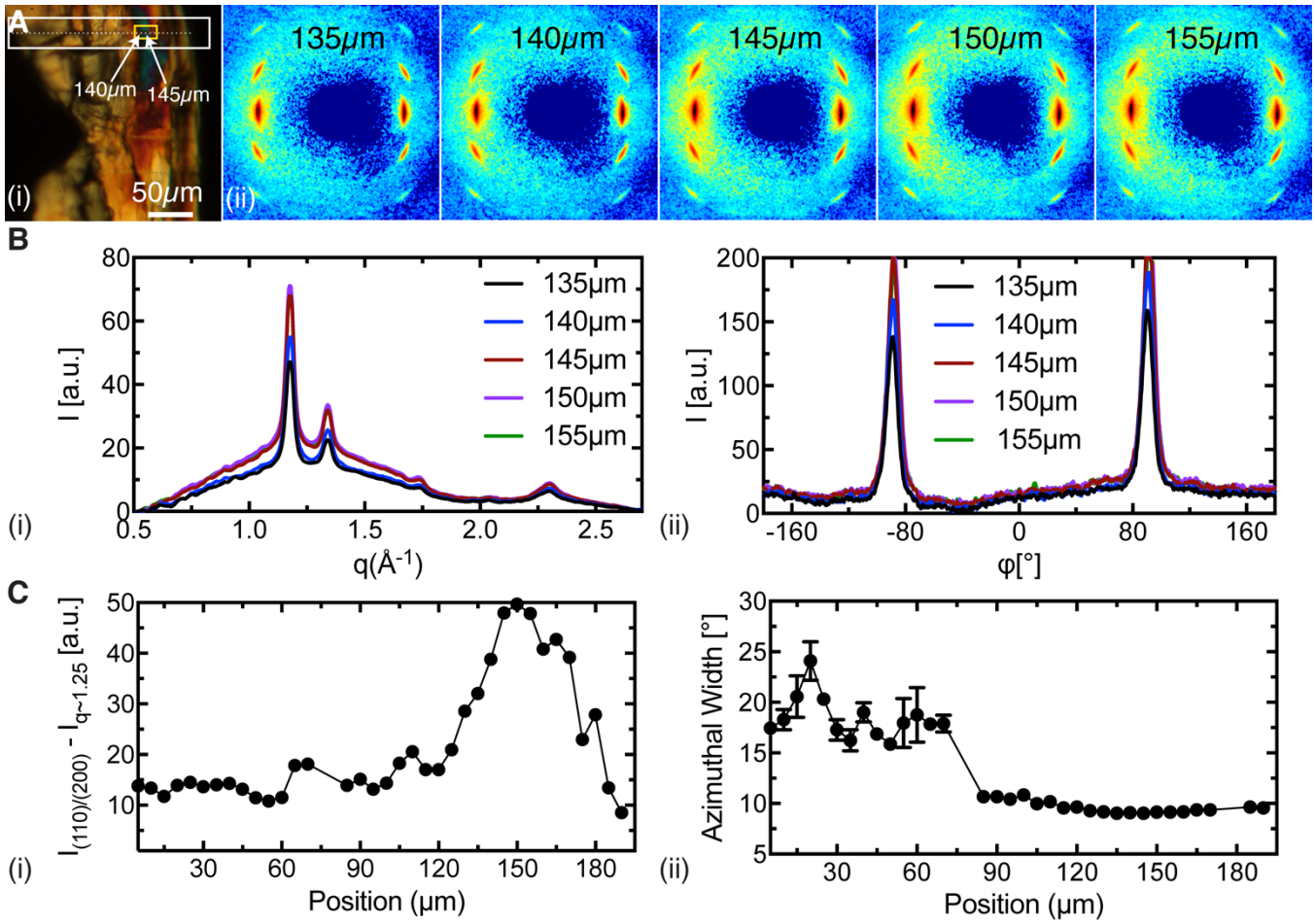

Fig. S7. Probing the morphology of high-retardance microdomains in the 18M scaffold using X-ray microdiffraction. The white box in the polarized light micrograph (*A*, i) highlights a line scan of microdiffraction data that passes through a high-retardance microdomain (region with blue-green Michel-Levy color). An array of points (dashed line inside the white box in *A*,i) is included to guide the eye along the microdiffraction line scan from the inner to the outer bend. The yellow box in (*A*, i) indicates a set of 5 diffraction patterns in the vicinity of the high-retardance microdomain. Diffraction patterns labeled 135, 140 and 155 μm (*A*, ii) lie adjacent to the microdomain, while diffraction patterns labeled 145 and 150 μm lie directly on the microdomain (the patterns are assigned distances relative to the inner bend of the section). The set of 5 diffraction patterns in (*A*, ii) are presented as (*B*, i) azimuthally averaged, I(q), and (*B*, ii) radially averaged, I(ϕ), plots. The complete line scan of microdiffraction data from the inner to the outer bend is analyzed to provide (*C*, i) an estimate of the crystallinity and (*C*, ii) the average azimuthal width at half maximum of the (110)/(200) diffraction peaks. The error bars in (*C*, ii), where visible, indicate the azimuthal widths of the two (110)/(200) peaks.

A striking feature of the morphology after 18 months of hydrolysis is non-uniformity: high-retardance microdomains (bright blue-green clusters, Fig. 1*D*, Fig. S2 and Fig. S7*A*, i) are observed in every microtomed section, interspersed with regions that possess much lower retardation (yellow to red Michel-Levy colors). Variations in retardation can arise due to changes in the degree of orientation or the amount of crystalline material. Microdiffraction data for the 18M sample show variations in the amount of crystalline material in the sample volume (see Fig. S7*B*, i and 90-180μm, Fig. S7*C*, i) — not variations in the degree of orientation (see Fig. S7*B*, ii and 90-180μm, Fig. S7*C*, ii). Thus, the bright blue-green

clusters that have retardation (>600 nm, 18M, Fig. 1*D*) higher than that observed anywhere in the 0M or 9M samples (<500 nm, Fig. 1*D*) must have a greater number of crystalline unit cells packed into the volume sampled in the microdiffraction beam.

It is known that hydrolysis of PLLA preferentially attacks non-crystalline segments (3–5); we hypothesize that there is an element of chance during hydrolysis regarding the fate of the non-crystalline segments affected by the scission of a bond in a tie chain or a loop. An increase in the number of crystalline unit cells can occur if a constraint that was preventing some segments from adding to an adjacent crystal is relieved by hydrolysis. We envision lamellar thickening, which adds unit cells with the same orientation as the lamellae they join. Where lamellar thickening occurs, transport of water in and lactic acid out may be hindered. On the other hand, the scission of a segment in the non-crystalline material facilitates transport of water in and lactic acid out, thereby increasing the removal of material. Depending on which of the two conditions occurs locally, the amount of crystalline material can either increase or decrease, leading to heterogeneities that were not present prior to hydrolysis.

Probing structural variations through the thickness of the 18M scaffold

For the section cut ~105 µm from the inner diameter of the 18M scaffold (Fig. S8*A*), we only present a low-magnification polarized light micrograph (Fig. S8*A*, i) as the sample fractured prior to high-magnification imaging. Using the scale bar, we assign the first X-ray pattern with distinct PLLA diffraction peaks to be ~5 µm from the inner bend of the section. The position of subsequent frames is known as the microdiffraction line scan has a 5µm spacing between consecutive diffraction patterns.

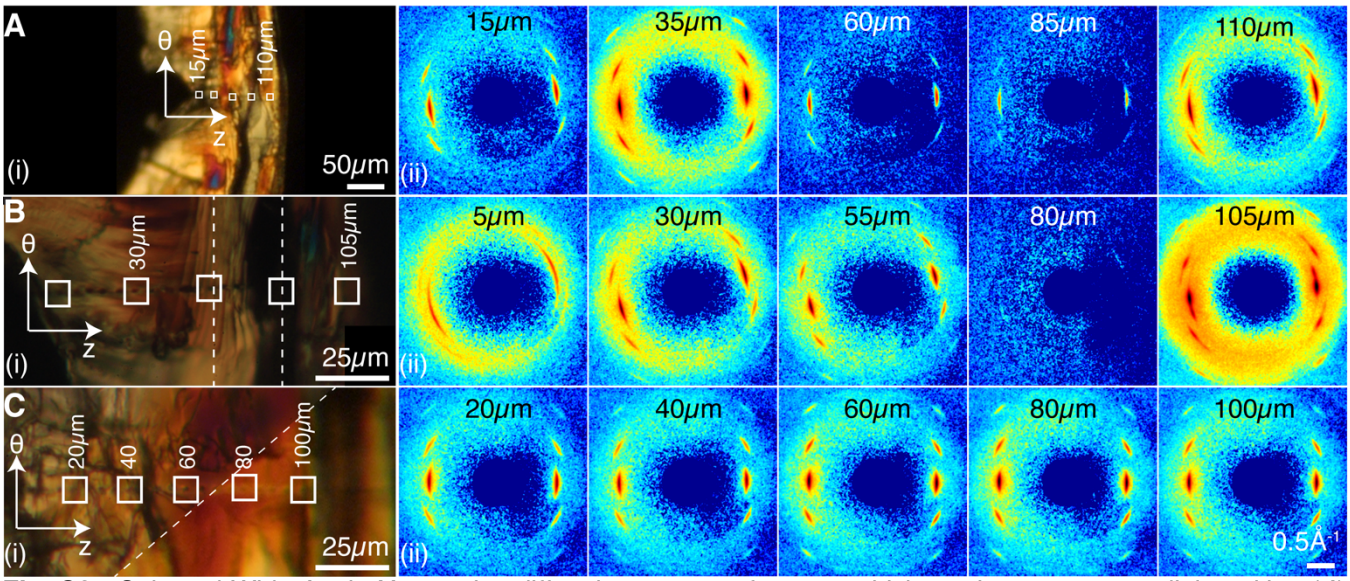

Fig. S8. Selected Wide-Angle X-ray microdiffraction patterns for 15*µ*m thick sections cut at a radial position (*A*) ~105*µ*m, (*B*) ~75*µ*m and (*C*) 60 *µ*m from the inner diameter of an 18-month hydrolyzed BVS (18M). (i) Polarized light micrographs show the position of microdiffraction acquisitions (white squares labelled with their distance from the inner bend correspond to patterns in (ii); white dashed lines indicate where images focused on specific X-ray marks were stitched together). (ii) 2D Diffraction patterns use an identical logarithmic color scale (colors vary from 0 [deep blue] to 3 [deep red] counts) and *q*-scale (indicated at bottom right). Measurements were made at beamline 2-ID-D at APS at Argonne National Labs. 1D plots corresponding to the 2D patterns above are presented in Figure S9.

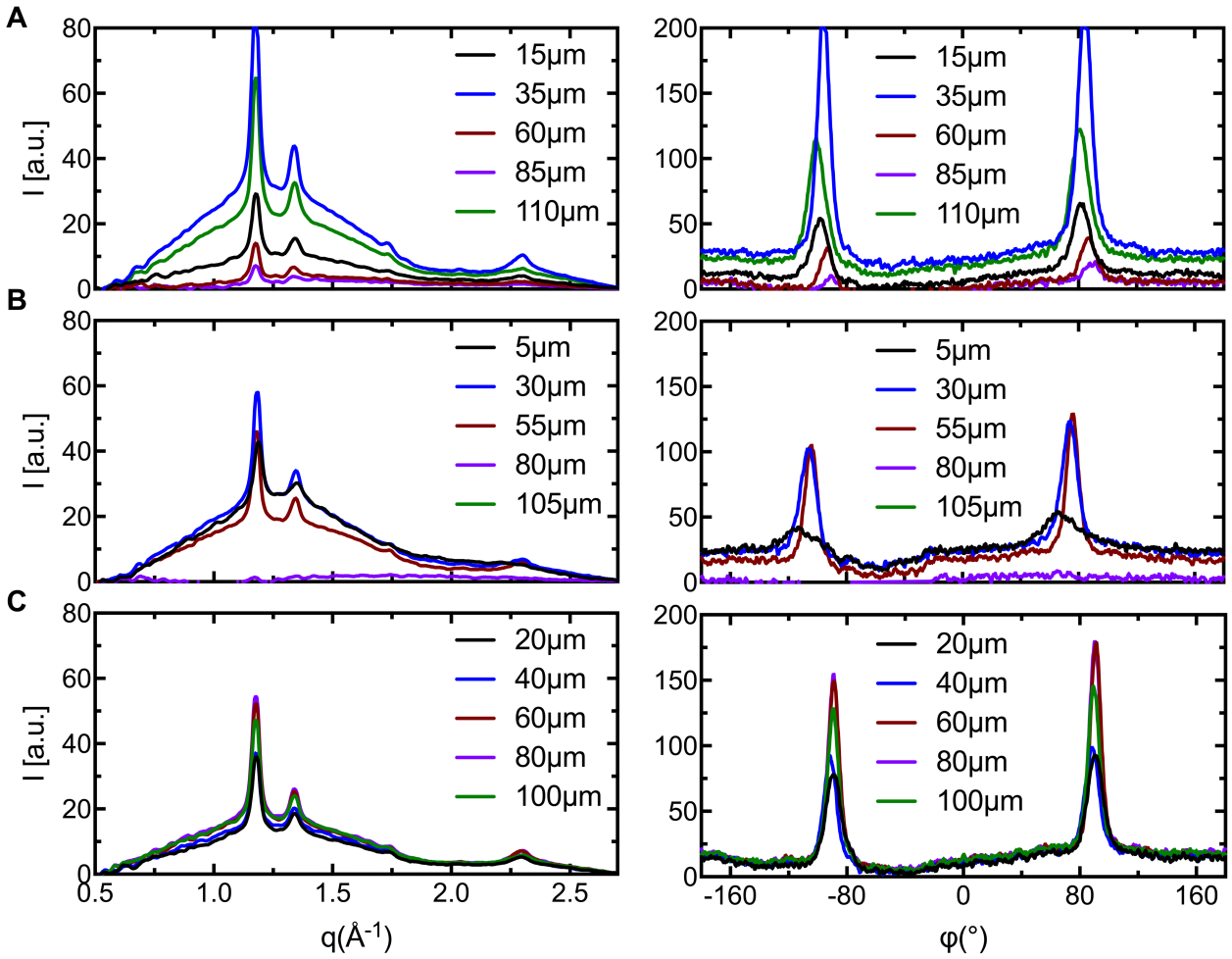

Fig. S9. Selected 1D microdiffraction profiles averaged (*left*) azimuthally, I(*q*), and (*right*) radially, I(*φ*) for the section taken (*A*) ~105 *µ*m, (*B*) ~75 *µ*m and (*C*) ~60 *µ*m from the inner diameter (ID) of an 18-month hydrolyzed BVS (18M). The position at which each X-ray pattern was acquired is indicated in the legend (same positions as the 2D patterns in Fig. S8). Radial averaging is performed in the vicinity of the (110)/(200) reflection: q∈ [1.08-1.24Å^{-1}]. Reduced 1D profiles of data acquired 105*µ*m from the IB of the section cut ~75*µ*m from the ID are not displayed as the material is this region is folded over, as evidenced by split (110)/(200) and (203) diffractions (see Fig. S8*B*, 105*µ*m).

Origin of the *r*-gradient in retardation in 0M and 9M scaffolds

Polarized light micrographs of sequential ~15 μm thick sections cut from as-deployed (0M) and 9-month hydrolyzed (9M) BVSs reveal an *r*-gradient in retardation through the thickness of the scaffold (see top to bottom in Figs. S3-S4). Such a gradient in the retardation could be due to a difference in the degree of crystallinity with fixed orientation distribution or to increased orientation with fixed degree of crystallinity or some combination. Wide angle X-ray diffraction is needed to discriminate among these possibilities. Microdiffraction data acquired on sections cut from different radial positions of the as-deployed BVS indicate a relatively low degree of crystallinity that hardly varies through the thickness of the 0M scaffold (Figs. S10-11 for X-ray data and Fig. S12*B* for quantitative characterization of crystallinity). Rather, the gradient in retardation correlates with a gradient in the degree of orientation of crystallites: the azimuthal width of the (110)/(200) diffraction peaks is substantially narrower at a radial position near the inner diameter (ID) compared to a section at the outer diameter (OD) of the scaffold (~28% narrower in a 0M section ~45μm from the ID relative to a 0M section ~105 μm from the ID, see 0M, Figs. S12*C*; ~50% narrower in a 9M section ~45μm from the ID relative to a 9M section ~135 μm from the ID, for 9M, compare Fig. S25*A-D*). We infer that the observed *r*-gradient in the orientation distribution of crystallites results from the gradient in hoop-strain during the tube expansion process, an important step in the manufacture of vascular scaffolds (6).

Tube expansion transforms an amorphous poly L-lactide (PLLA) preform into a semicrystalline tube that is laser-cut and crimped onto a balloon catheter, which is subsequently surgically positioned at the lesion and the BVS is deployed. The PLLA preform is heated in excess of 70°C (Tg ~ 55-60°C) inside a mold and is subjected to rapid deformation (7). The mold limits the extent of deformation (OD~3.5 mm) and rapidly quenches the sample due to the large thermal mass of the mold relative to the thin layer of polymer (thickness~150μm) and the low temperature of the mold (below Tg). The rapid quenching of the expanded PLLA tube can explain the observed low crystallinity of as-deployed BVSs (Fig. S12*B*). The imposed strain varies significantly with radial position: the extruded preform typically has an OD that is more than twice the ID and both of these diameters stretch to approximately the same final length (expanded tube OD is less than 10% greater than ID) (6). Specifically, tube expansion subjects PLLA near the OD to relatively mild strains of ~100%, while PLLA near the ID stretches in excess of 400% (6) (the axial elongation is small and independent of radial position). The gradient in hoop strain results in a gradient of morphology in the expanded tube: the degree of orientation of crystallites increases from the OD to the ID of the expanded tube and, consequently, of the as deployed scaffold.

Probing structural variations through the thickness of the as-deployed (0M) scaffold

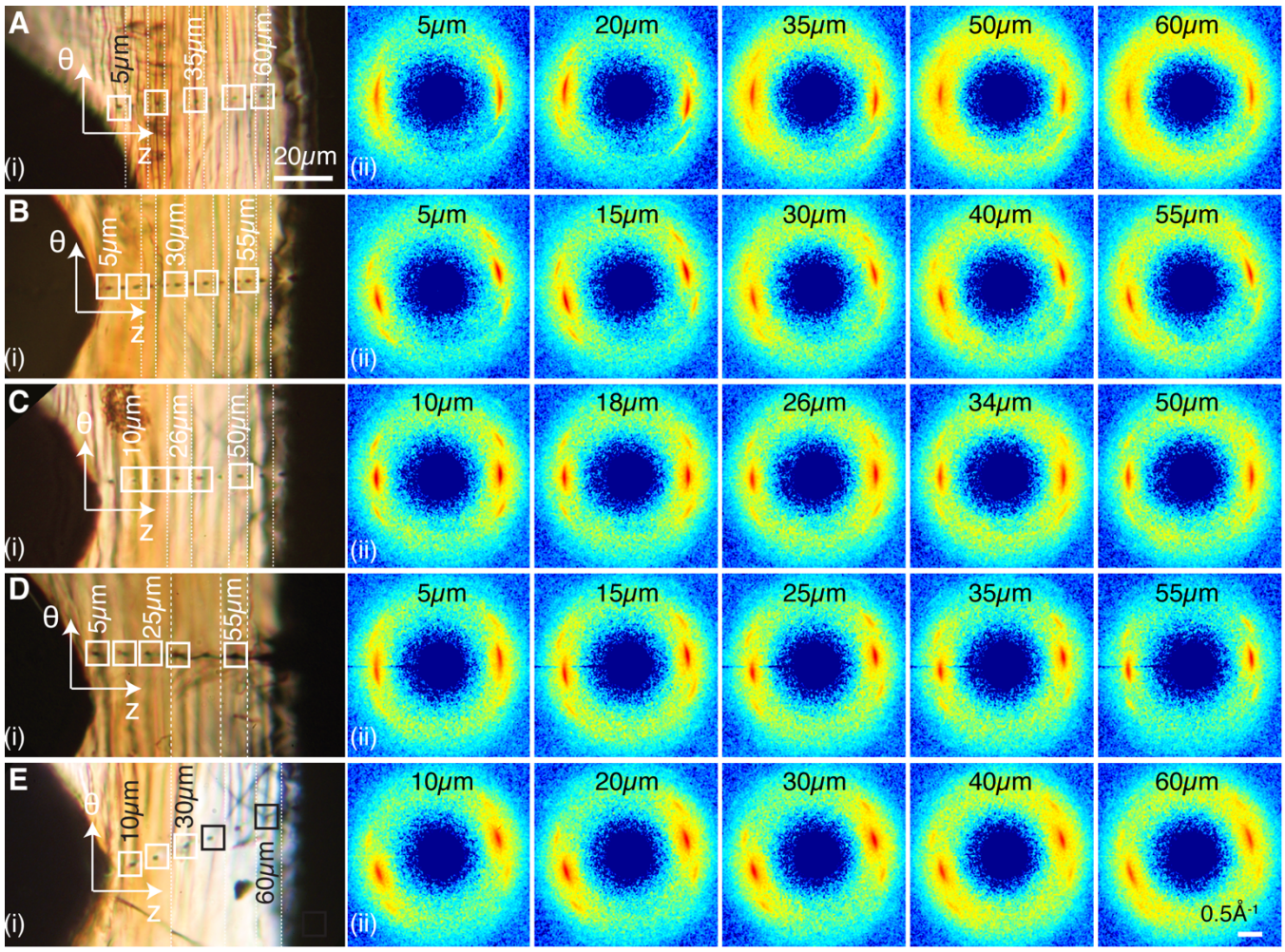

Fig. S10. Selected Wide-Angle X-ray microdiffraction patterns for ~15 μm thick sections cut at a radial position (A) ~105 μm, (B) ~90 μm, (C) ~75 μm, (D) ~60 μm and (E) ~45 μm from the inner diameter of an as-deployed BVS (0M). (i) Polarized light micrographs show the position of microdiffraction acquisitions (white squares labelled with their distance from the inner bend correspond to patterns in (ii); white dashed lines indicate where images focused on specific X-ray marks were stitched together). (ii) 2D Diffraction patterns use an identical logarithmic color scale (colors vary from 0 [deep blue] to 3 [deep red] counts) and q-scale (indicated at bottom right). Measurements were made at beamline 2-ID-D at APS at Argonne National Labs. 1D plots corresponding to the 2D patterns above are presented in Figure S11.

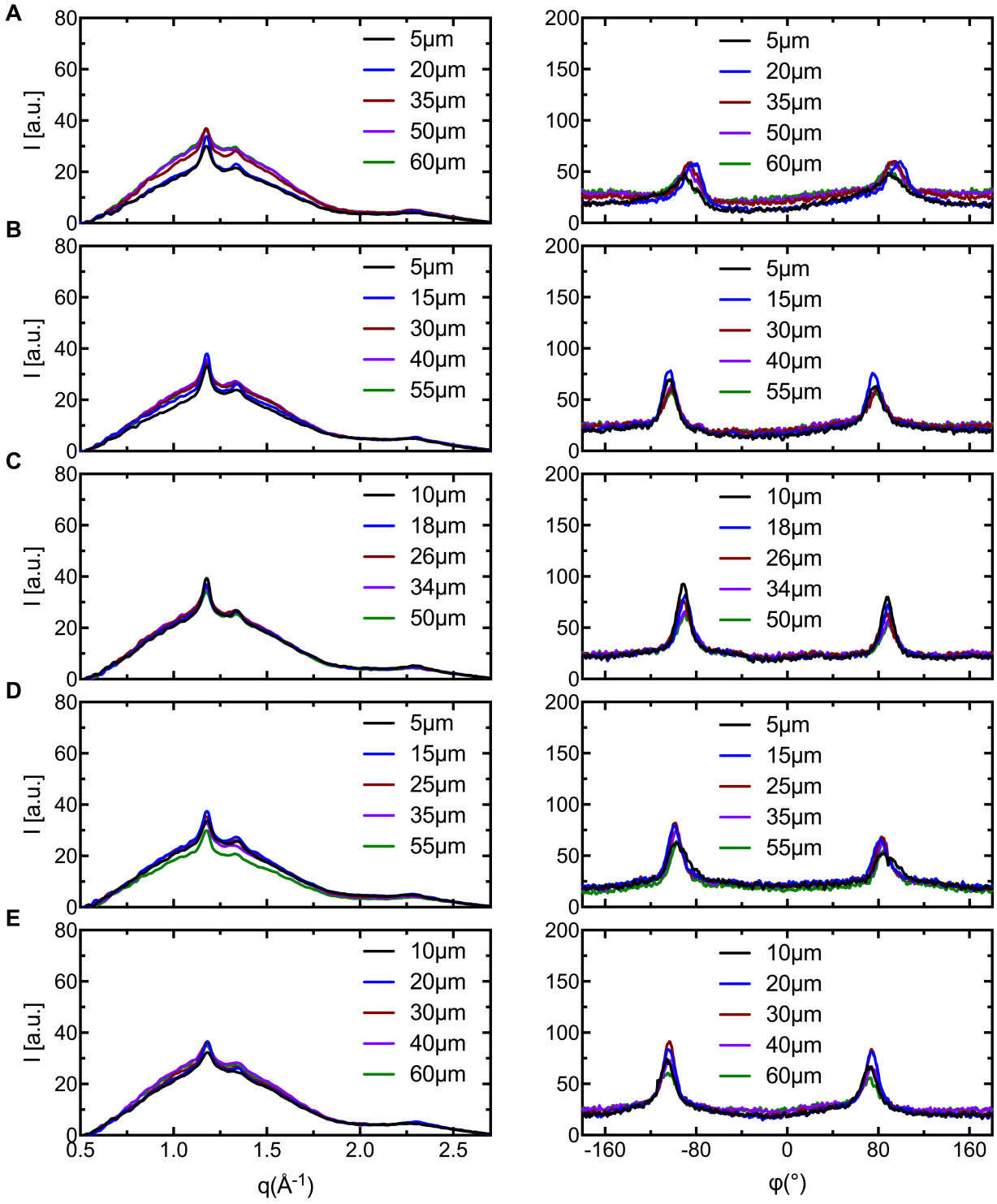

Fig. S11. Selected 1D microdiffraction profiles averaged (*left*) azimuthally, I(*q*), and (*right*) radially, I(*φ*) for the section taken (*A*) ~105 *μ*m, (*B*) ~90 *μ*m, (*C*) ~75 *μ*m, (*D*) ~60 *μ*m, and (*E*) ~45*μ*m from the inner diameter of an as-deployed BVS (0M). The position at which each X-ray pattern was acquired is indicated in the legend (same positions as the 2D patterns in Fig. S10). Radial averaging was performed in the vicinity of the (110)/(200) reflection: $q \in [1.08\text{-}1.24 Å^{-1}]$.

Quantitative characteristics of ~15µm thick sections cut from the 0M scaffold

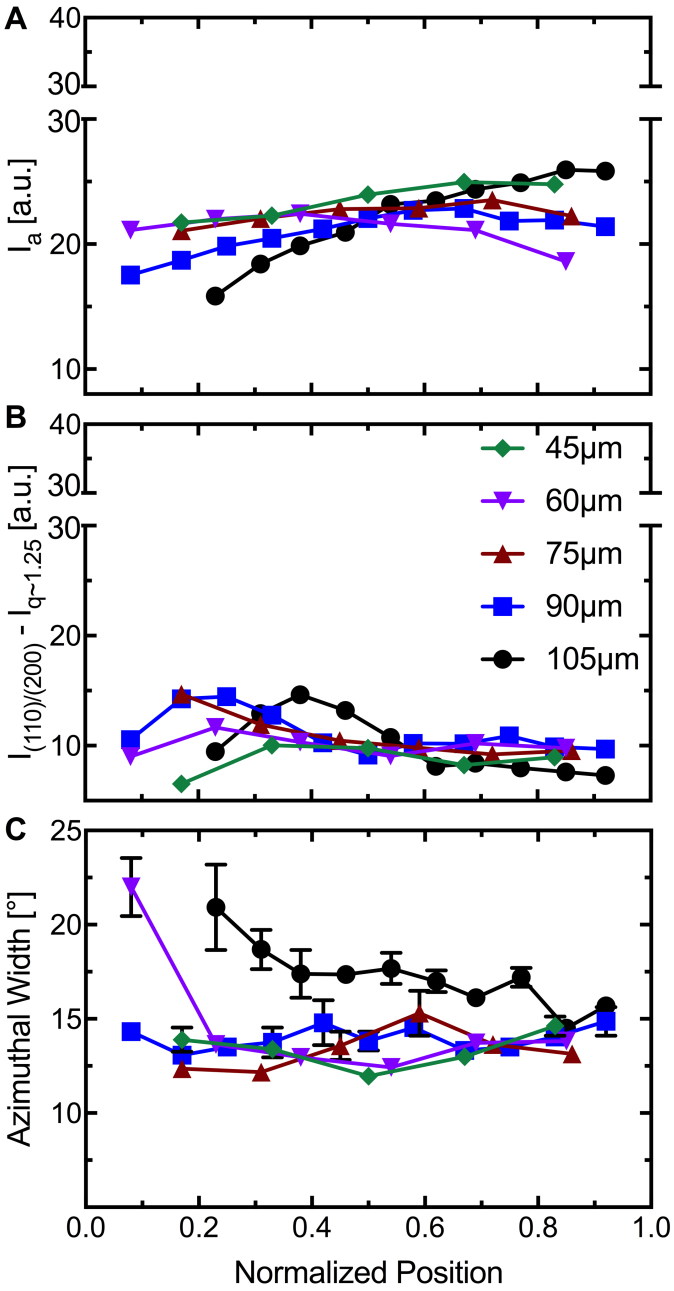

Fig. S12. Quantitative characteristics of microdiffraction data acquired on sections cut ~105μm, ~90μm, ~75μm, ~60μm and ~45μm from the ID of an as-deployed (0M) scaffold (see Fig. S10 for 2D patterns). The azimuthally and radially averaged intensity (Fig. S11) are used to compute (*A*) the intensity of the noncrystalline halo, I_a averaged over $q \in [0.95\text{-}1.05\text{Å}^{-1}]$, (*B*) the intensity associated with crystalline diffraction, $I_{max,(110)/(200)} - I_{q\sim1.25}$, and (*C*) full-width at half maximum of the (110)/(200) peaks.

Microstructure of the section cut ~135µm from the inner diameter of the 9M scaffold

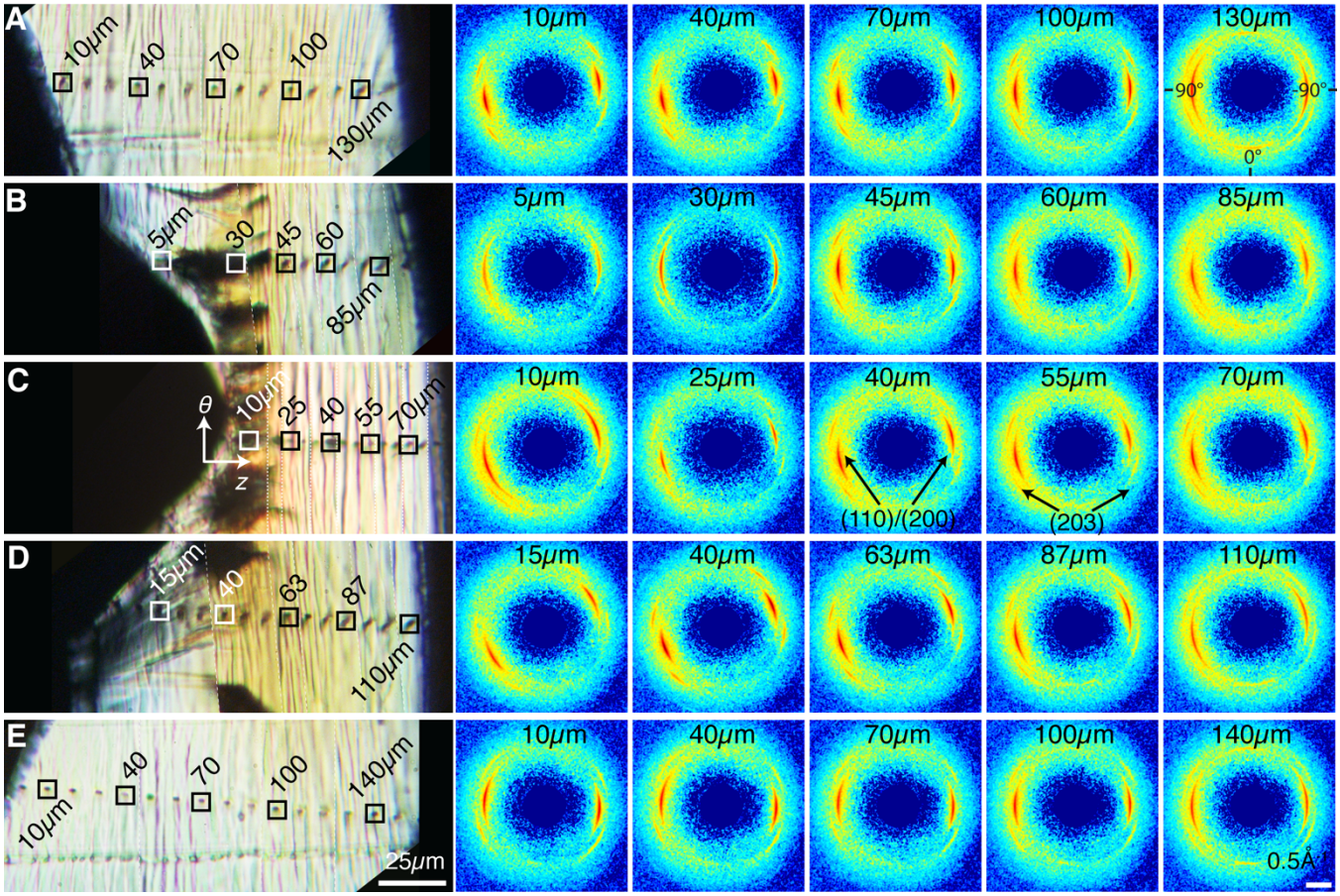

Fig. S13. Selected Wide-Angle X-ray microdiffraction patterns acquired 180µm (*A* and *E*) and 50µm (*B* and *D*) from the (*C*) symmetry plane of the section cut ~135µm from the ID of a 9M scaffold. (i) Polarized light micrographs show the position of microdiffraction acquisitions (squares labelled with their distance from the inner bend correspond to patterns in (ii); white dashed lines indicate where images focused on specific X-ray marks were stitched together). (ii) 2D Diffraction patterns use an identical logarithmic color scale (colors vary from 0 [deep blue] to 3 [deep red]) and *q*-scale (indicated at bottom right). Measurements were made at APS beamline 2-ID-D at Argonne National Labs. 1D plots corresponding to the 2D patterns above are presented in Figure S18.

Microstructure of the section cut ~120µm from the inner diameter of the 9M scaffold

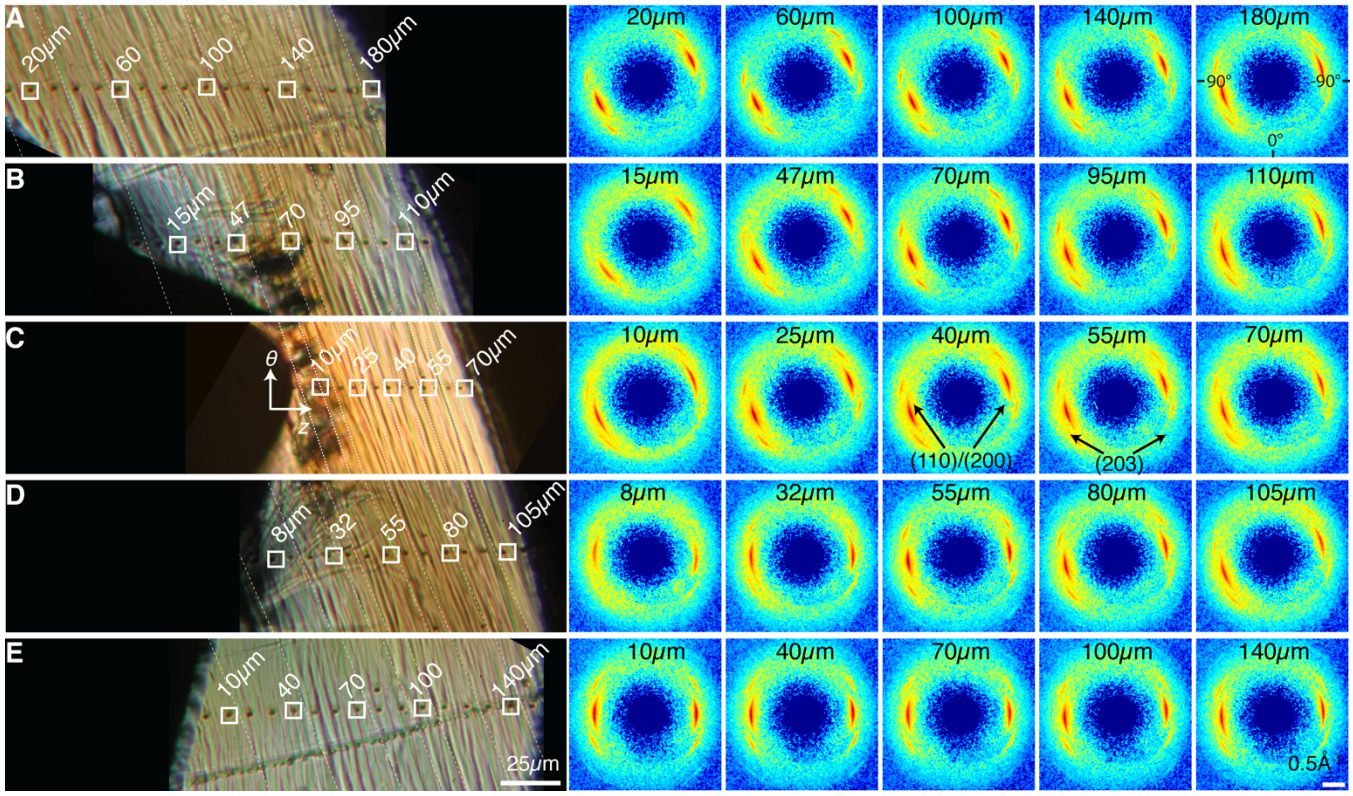

Fig. S14. Selected Wide-Angle X-ray microdiffraction patterns acquired 180*µ*m (*A* and *E*) and 60*µ*m (*B* and *D*) from the (*C*) symmetry plane of the section cut ~120*µ*m from the ID of a 9M scaffold. (i) Polarized light micrographs show the position of microdiffraction acquisitions (squares labelled with their distance from the inner bend correspond to patterns in (ii); white dashed lines indicate where images focused on specific X-ray marks were stitched together). (ii) 2D Diffraction patterns use an identical logarithmic color scale (colors vary from 0 [deep blue] to 3 [deep red]) and *q*-scale (indicated at bottom right). Measurements were made at APS beamline 2-ID-D at Argonne National Labs. 1D plots corresponding to the 2D patterns above are presented in Figure S19.

Microstructure of the section cut ~60µm from the inner diameter of the 9M scaffold

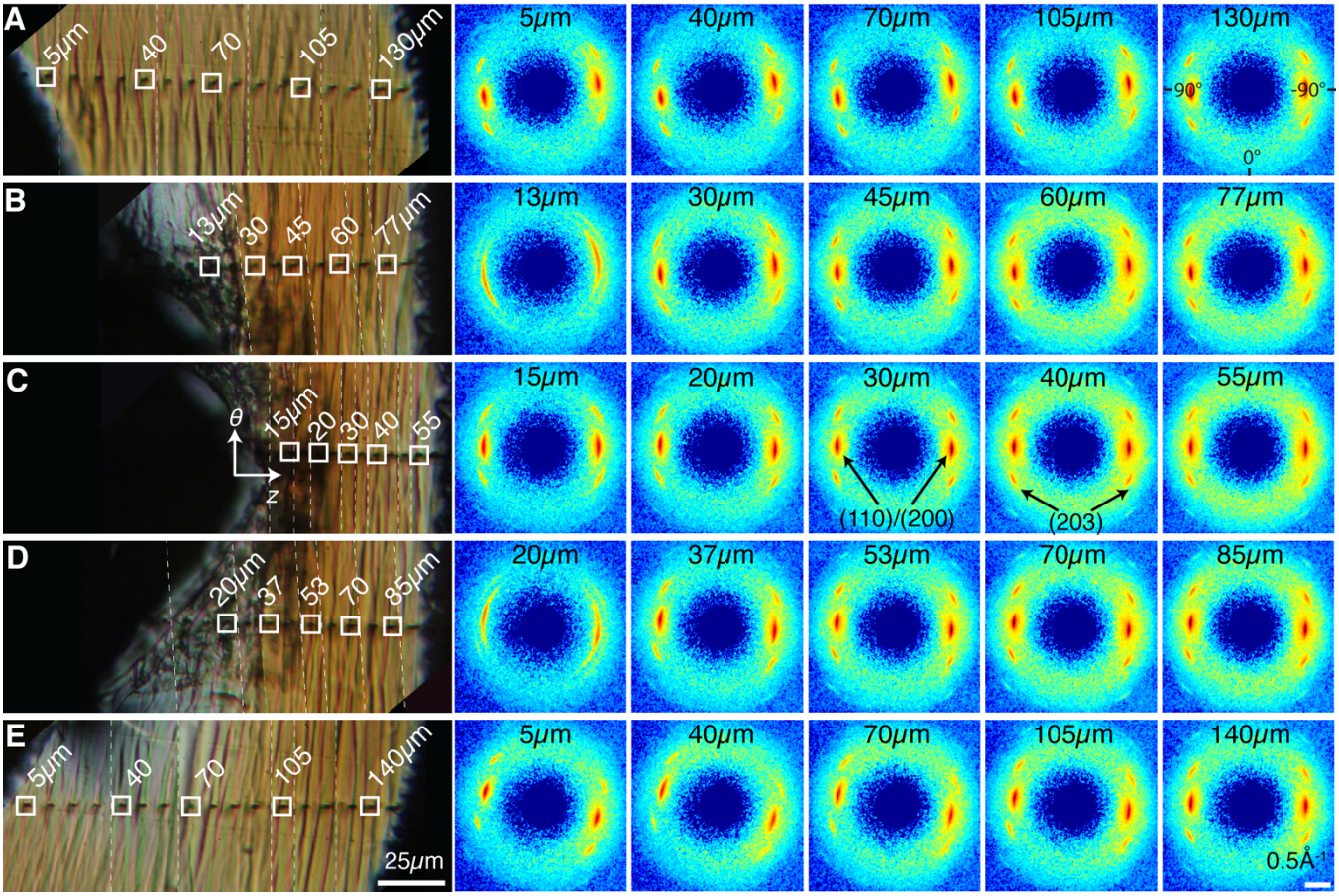

Fig. S15. Selected Wide-Angle X-ray microdiffraction patterns acquired 180*µ*m (*A* and *E*) and 60*µ*m (*B* and *D*) from the (*C*) symmetry plane of the section cut ~60*µ*m from the ID of a 9M scaffold. (i) Polarized light micrographs show the position of microdiffraction acquisitions (squares labelled with their distance from the inner bend correspond to patterns in (ii); white dashed lines indicate where images focused on specific X-ray marks were stitched together). (ii) 2D Diffraction patterns use an identical logarithmic color scale (colors vary from 0 [deep blue] to 3 [deep red]) and *q*-scale (indicated at bottom right). Measurements were made at APS beamline 2-ID-D at Argonne National Labs. 1D plots corresponding to the 2D patterns above are presented in Figure S20.

Microstructure of the section cut ~45µm from the inner diameter of the 9M scaffold

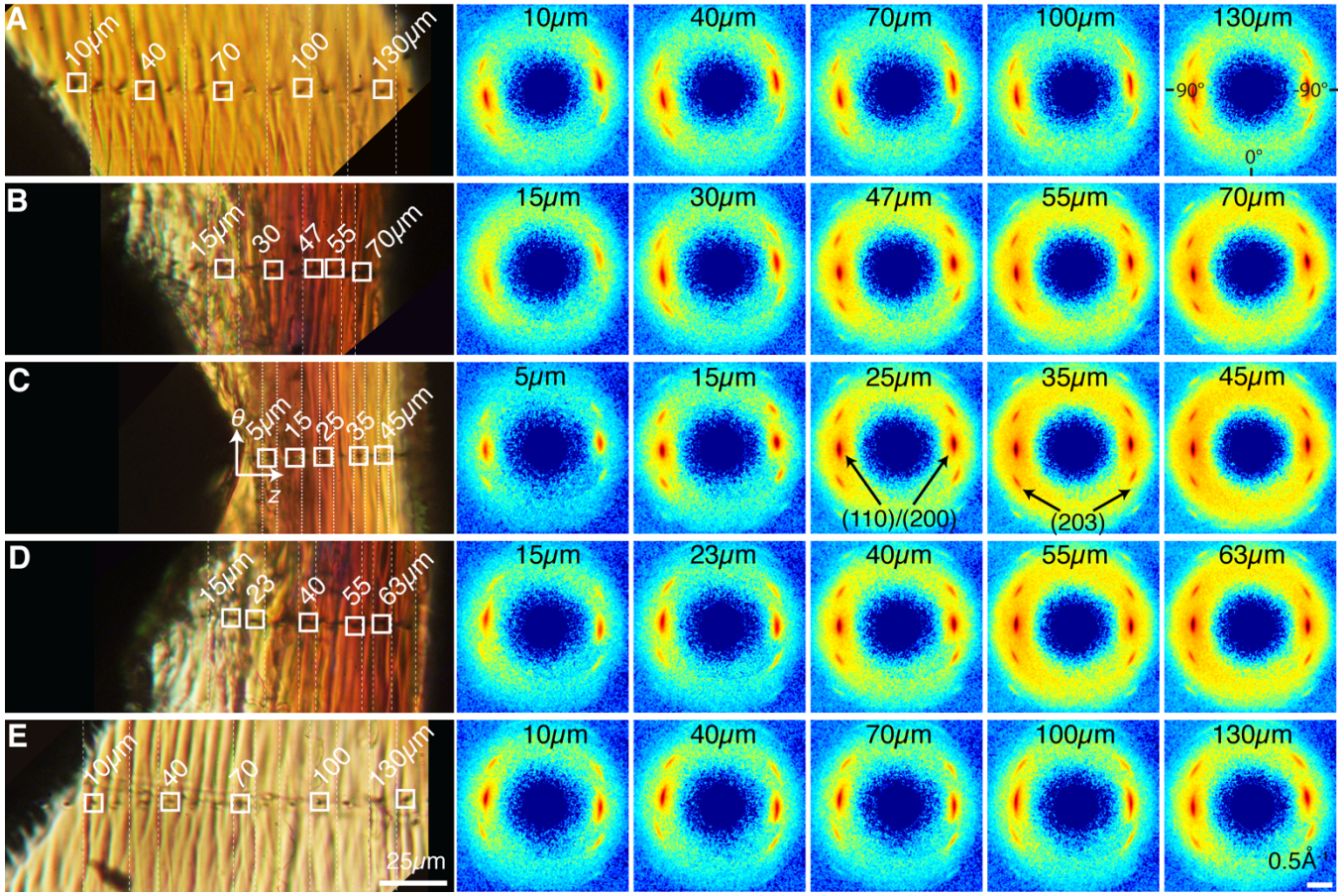

Fig. S16. Selected Wide-Angle X-ray microdiffraction patterns acquired (*A*) 240*µ*m and (*E*) 200*µ*m above and below the symmetry plane respectively, and 60*µ*m (*B* and *D*) from the (*C*) symmetry plane of the section cut ~45 *µ*m from the ID of a 9M scaffold. (i) Polarized light micrographs show the position of microdiffraction acquisitions (squares labelled with their distance from the inner bend correspond to patterns in (ii); white dashed lines indicate where images focused on specific X-ray marks were stitched together). (ii) 2D Diffraction patterns use an identical logarithmic color scale (colors vary from 0 [deep blue] to 3 [deep red]) and *q*-scale (indicated at bottom right). Measurements were made at APS beamline 2-ID-D at Argonne National Labs. 1D plots corresponding to the 2D patterns above are presented in Figure S21.

Microstructure of the section cut ~15µm from the inner diameter of the 9M scaffold

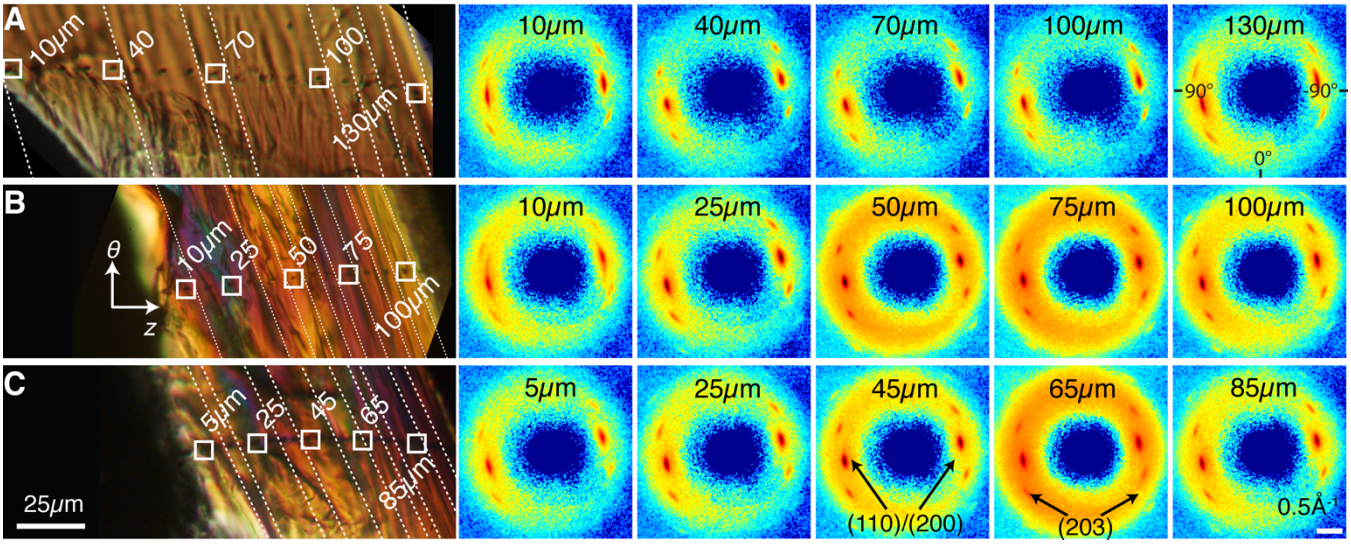

Fig. S17. Selected Wide-Angle X-ray microdiffraction patterns acquired (*A*) 200*µ*m and (*C*) 60*µ*m from the (*B*) symmetry plane of the section cut ~15 *µ*m from the ID of a 9M scaffold. (i) Polarized light micrographs show the position of microdiffraction acquisitions (squares labelled with their distance from the inner bend correspond to patterns in (ii); white dashed lines indicate where images focused on specific X-ray marks were stitched together). (ii) 2D Diffraction patterns use an identical logarithmic color scale (colors vary from 0 [deep blue] to 3 [deep red]) and *q*-scale (indicated at bottom right). Measurements were made at APS beamline 2-ID-D at Argonne National Labs. 1D plots corresponding to the 2D patterns above are presented in Figure S22.

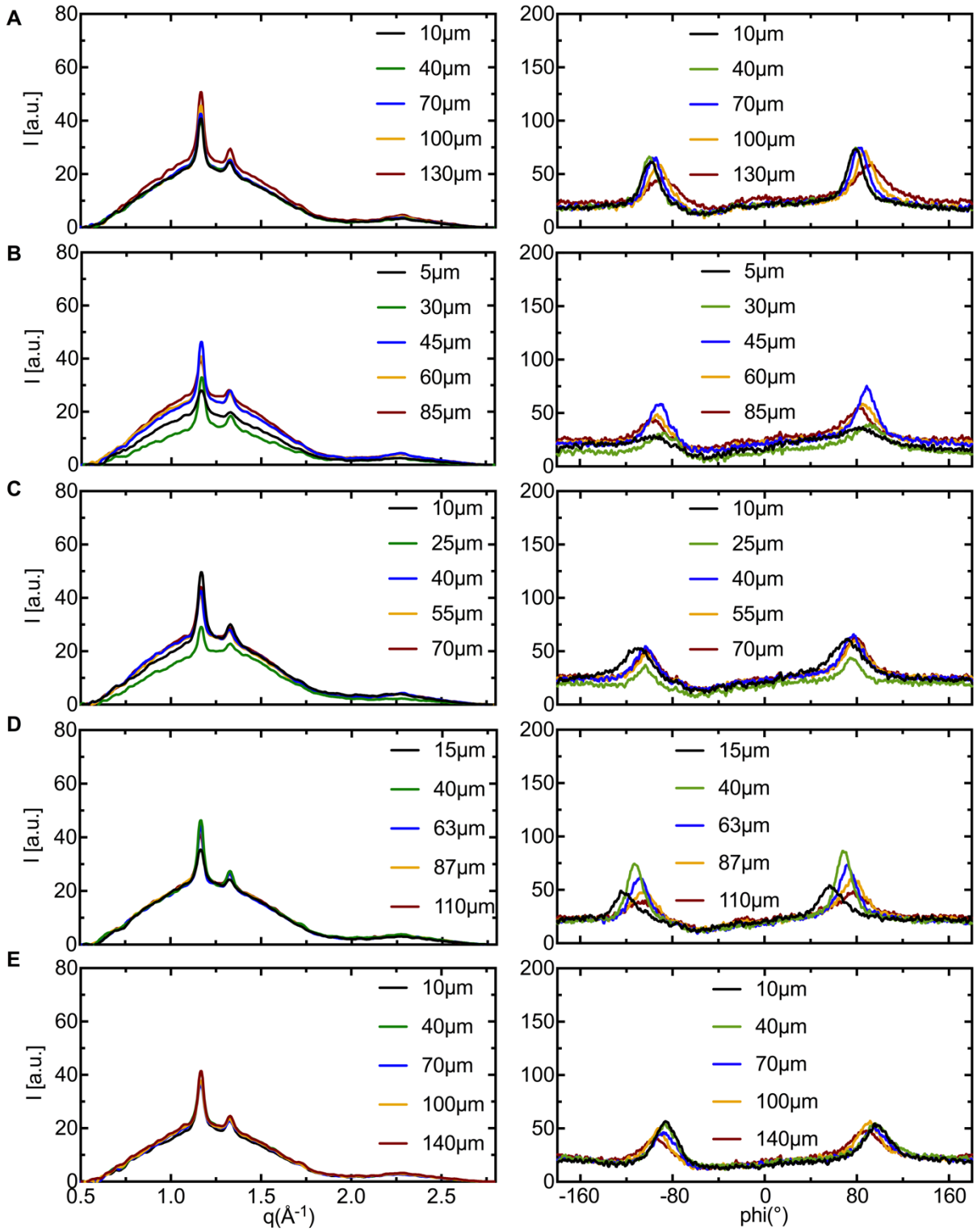

Fig. S18. Selected 1D microdiffraction profiles averaged (*left*) azimuthally, I(*q*), and (*right*) radially, I(*ϕ*) for WAXS patterns acquired along the arms (*A* and *E*) and (*B* and *D*) 50*μ*m from the (*C*) symmetry plane of the section cut ~135*μ*m from the ID of a 9M scaffold. The 1D plots correspond to the 2D patterns presented in Figure S13. Radial averaging was performed in the vicinity of the (110)/(200) reflection: $q \in [1.08\text{-}1.24 Å^{-1}]$.

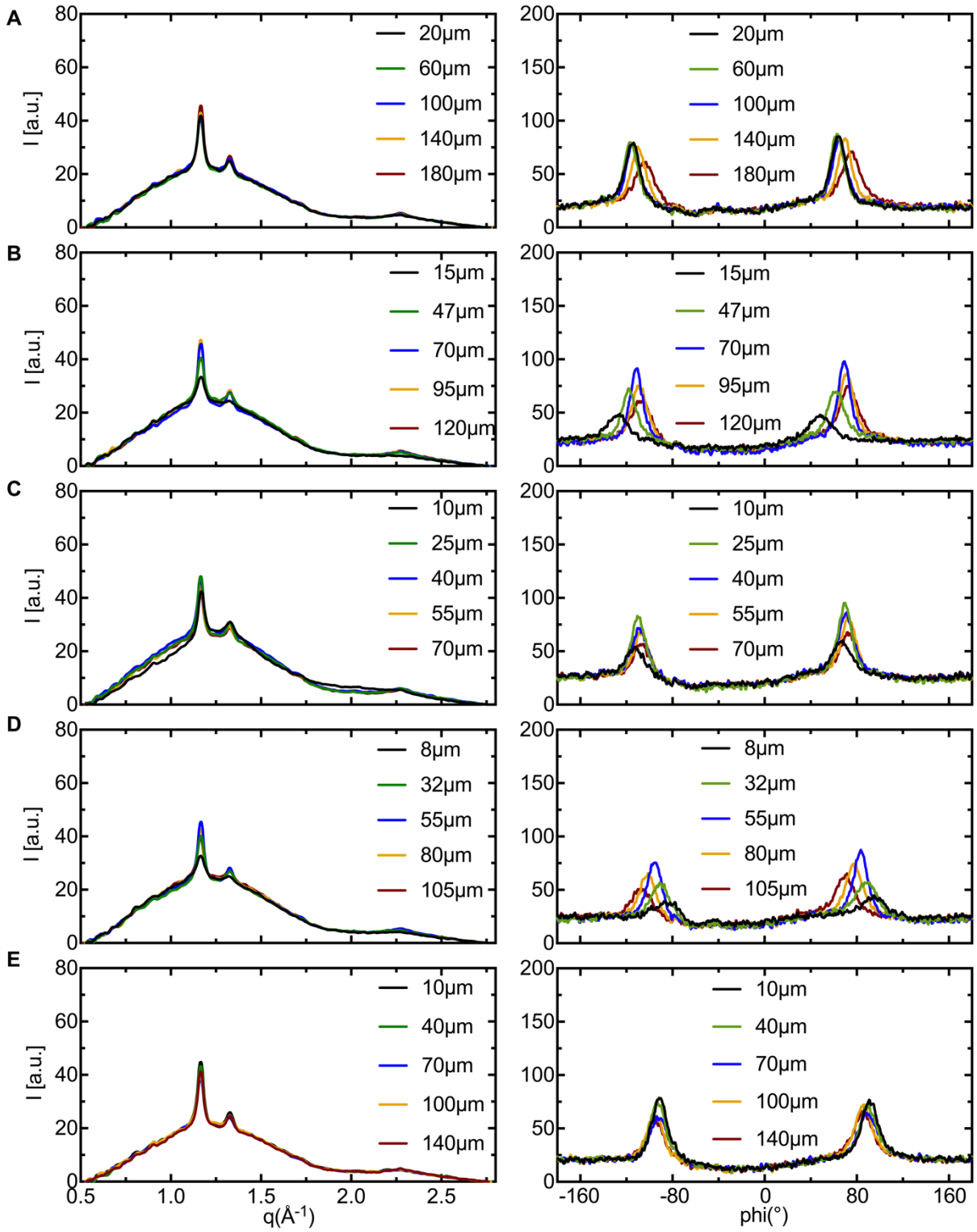

Fig. S19. Selected 1D microdiffraction profiles averaged (*left*) azimuthally, I(*q*), and (*right*) radially, I(*ϕ*) for WAXS patterns acquired along the arms (*A* and *E*) and (*B* and *D*) 60*μ*m from the (*C*) symmetry plane of the section cut ~120*μ*m from the ID of a 9M scaffold. The 1D plots correspond to the 2D patterns presented in Figure S14. Radial averaging was performed in the vicinity of the (110)/(200) reflection: $q \in [1.08\text{-}1.24 Å^{-1}]$.

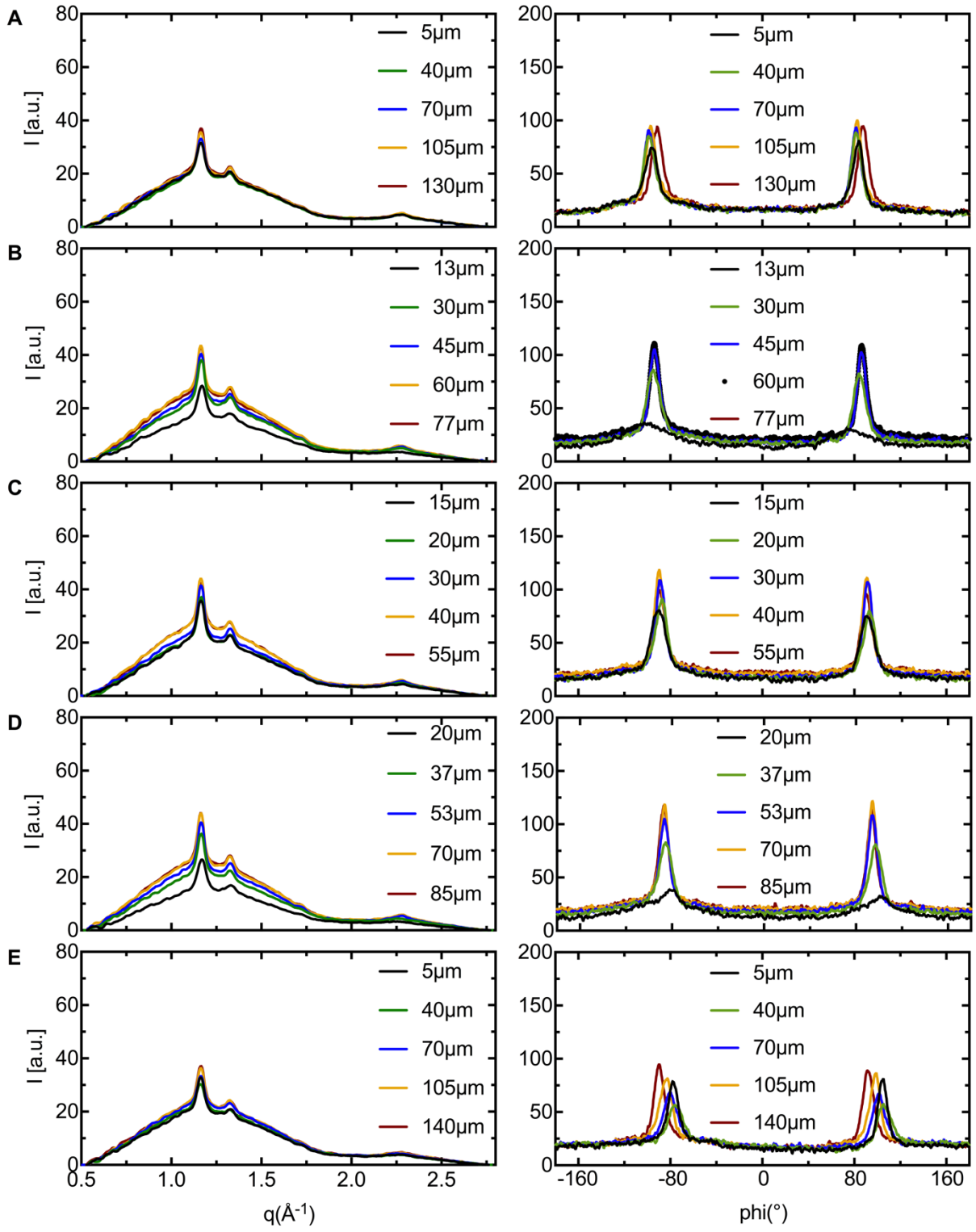

Fig. S20. Selected 1D microdiffraction profiles averaged (*left*) azimuthally, I(*q*), and (*right*) radially, I(*ϕ*) for WAXS patterns acquired along the arms (*A* and *E*) and (*B* and *D*) 60*μ*m from the (*C*) symmetry plane of the section cut ~60*μ*m from the ID of a 9M scaffold. The 1D plots correspond to the 2D patterns presented in Figure S15. Radial averaging was performed in the vicinity of the (110)/(200) reflection: $q \in [1.08\text{-}1.24 Å^{-1}]$.

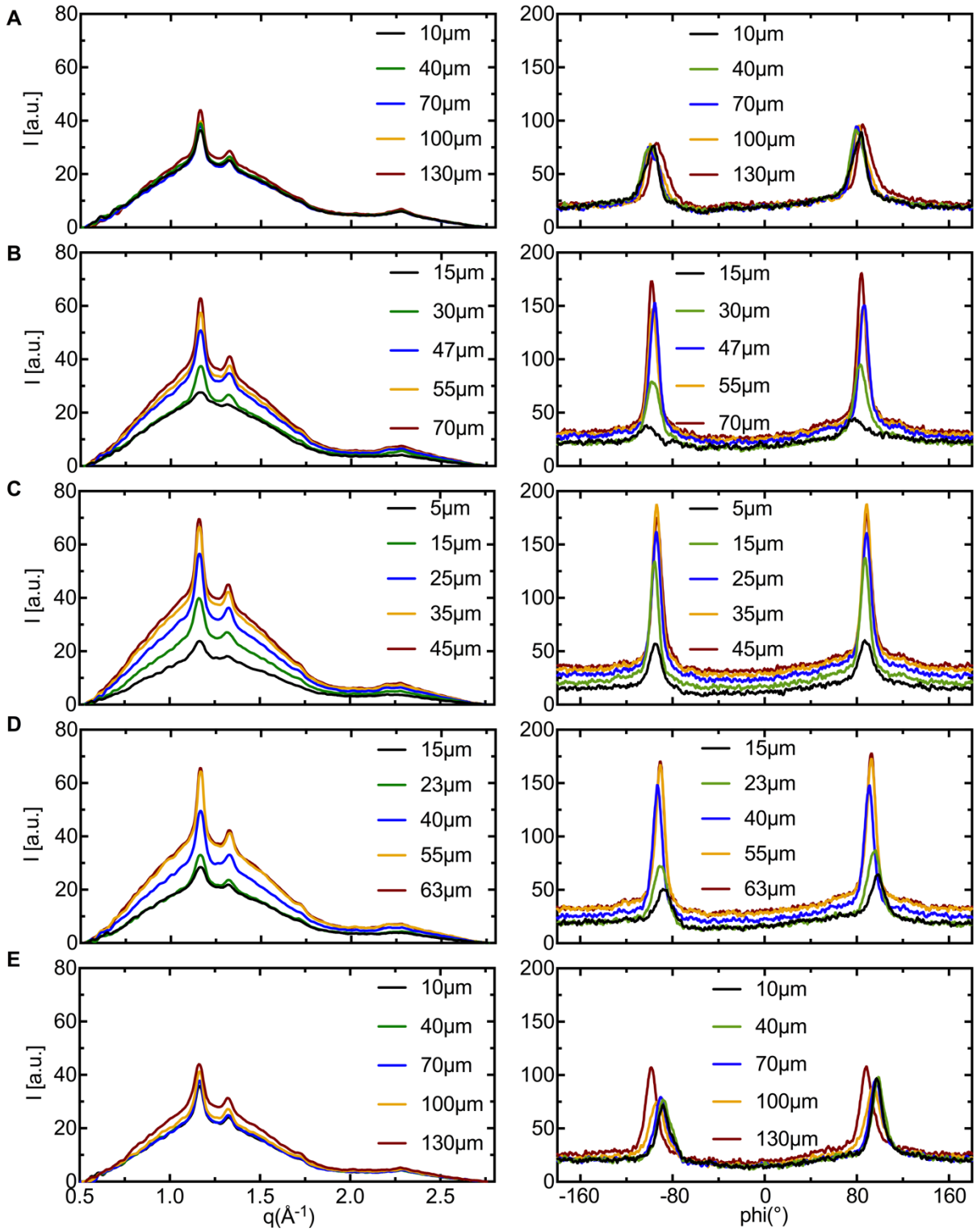

Fig. S21. Selected 1D microdiffraction profiles averaged (*left*) azimuthally, I(*q*), and (*right*) radially, I(*ϕ*) for WAXS patterns acquired along the arms (*A* and *E*) and (*B* and *D*) 60*µ*m from the (*C*) symmetry plane of the section cut ~45*µ*m from the ID of a 9M scaffold. The 1D plots correspond to the 2D patterns presented in Figure S16. Radial averaging was performed in the vicinity of the (110)/(200) reflection: $q \in [1.08\text{-}1.24 Å^{-1}]$.

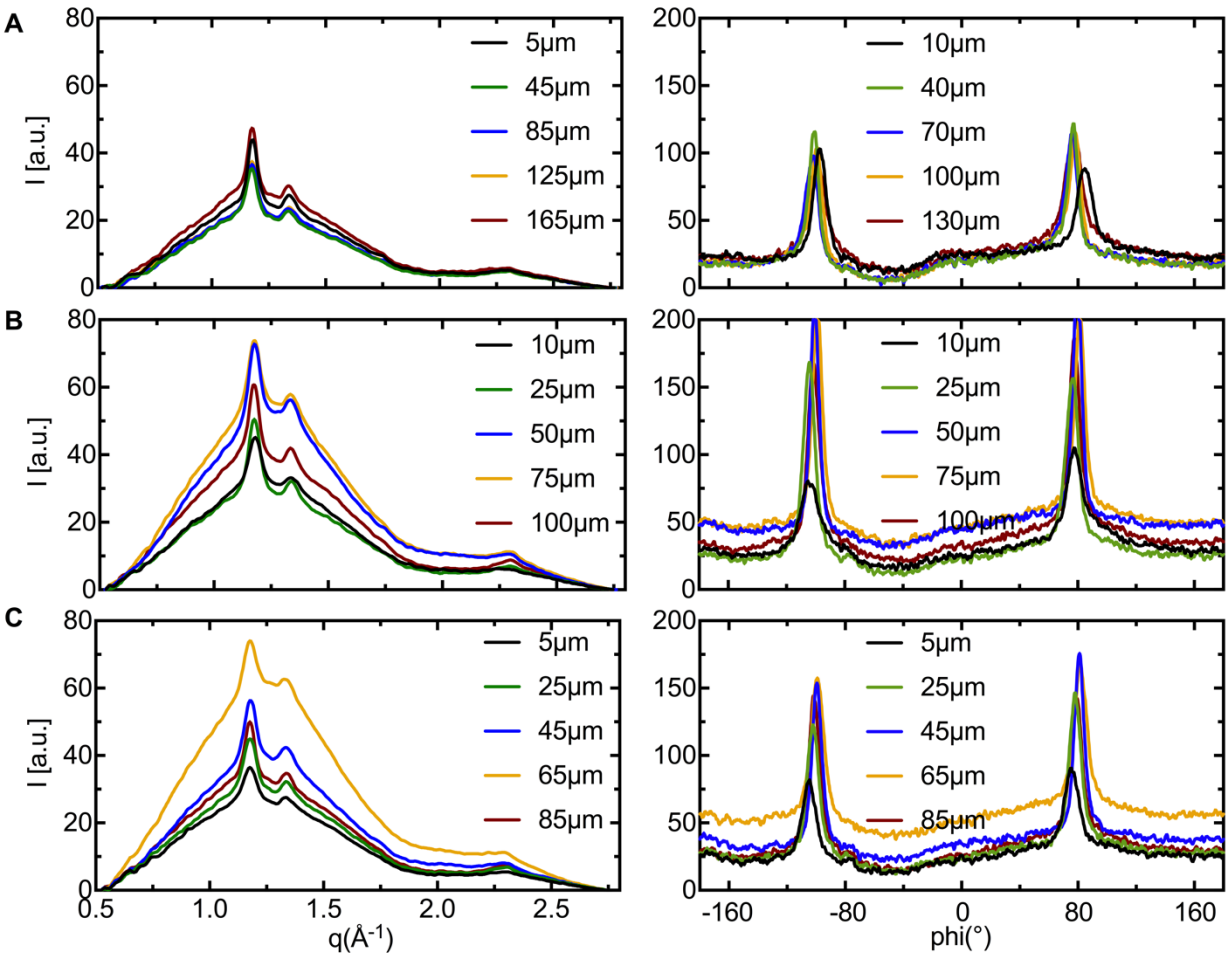

Fig. S22. Selected 1D microdiffraction profiles averaged (*left*) azimuthally, I(*q*), and (*right*) radially, I(*ϕ*) for WAXS patterns acquired along the arms (*A*) and (*C*) ~60*μ*m from the (*B*) symmetry plane of the section cut ~15*μ*m from the ID of a 9M scaffold. The 1D plots correspond to the 2D patterns presented in Figure S17. Radial averaging was performed in the vicinity of the (110)/(200) reflection: $q \in [1.08\text{-}1.24 Å^{-1}]$.

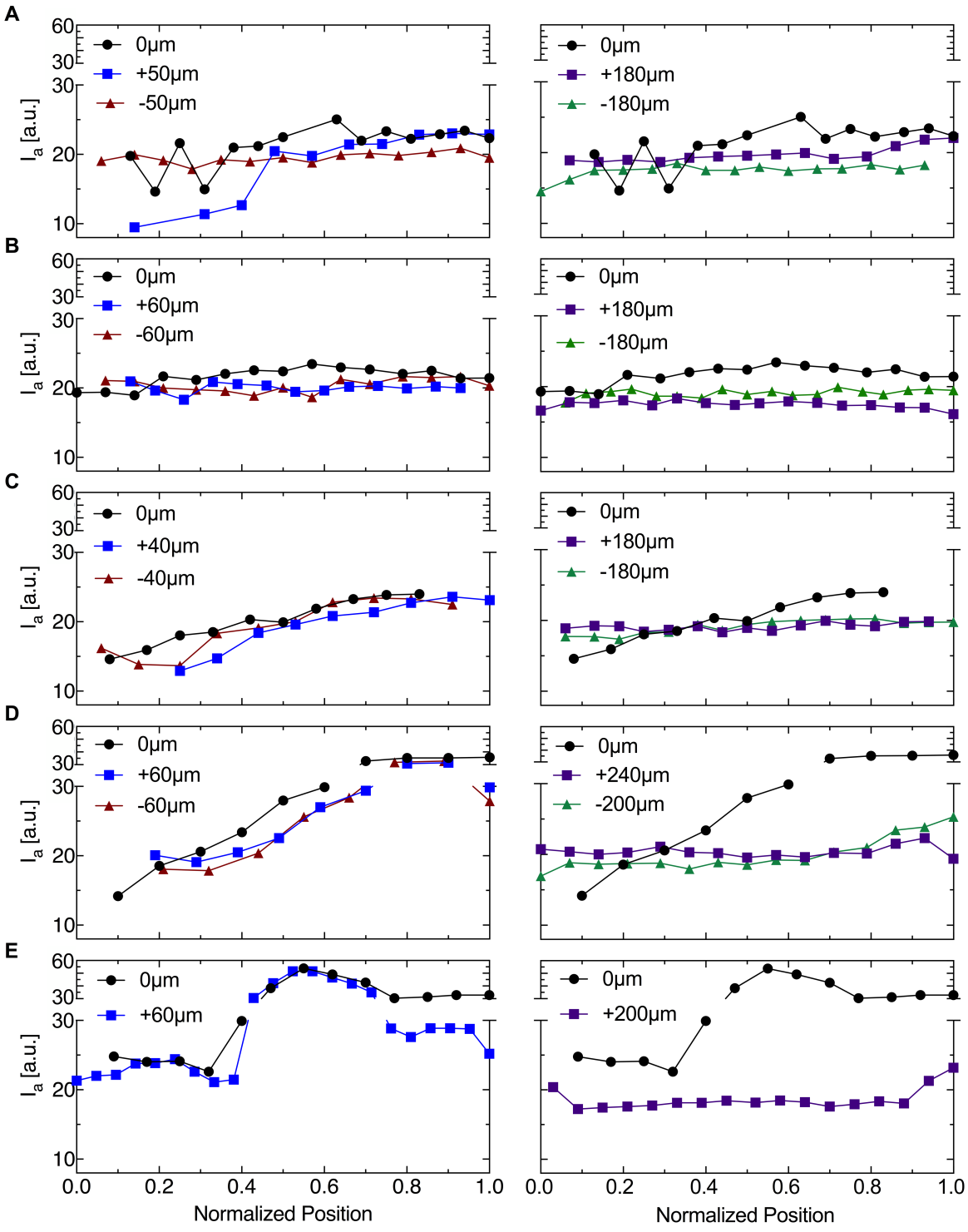

Fig. S23. The amorphous content (*left*) near the symmetry plane and (*right*) along the arms is presented for sections cut (*A*) ~135*μ*m, (*B*) ~120*μ*m, (*C*) ~60*μ*m (*D*) ~45*μ*m and (*E*) ~15*μ*m from the ID of a 9M scaffold (see Figs. S13–S22 for X-ray data). The legend (e.g. +60*μ*m or -180*μ*m) indicates the position of the line scan relative to the symmetry plane of the section. The amorphous content represents the mean of the azimuthally averaged intensity between $q \in [0.95 - 1.05]$ Å^{-1}. Normalized position varies from 0 at the inner bend (IB) to 1 at outer bend (OB).

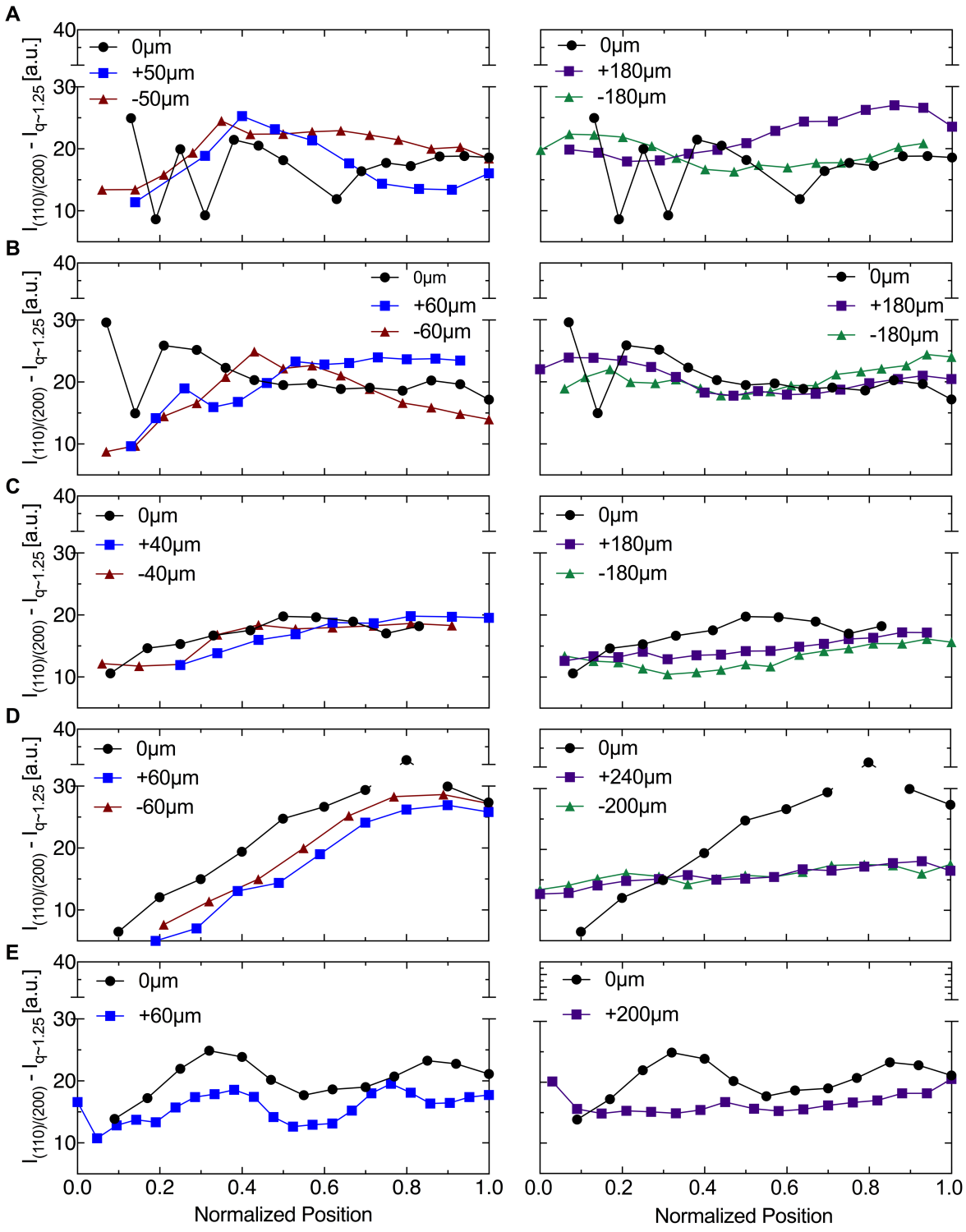

Fig. S24. The difference in intensity between the (110)/(200) peaks ($q \sim 1.17$Å^{-1}) and the halo at $q \sim 1.25$Å^{-1} ($I_{(110)/(200)} - I_{q\sim1.25}$) is a measure of the crystallinity (*left*) near the symmetry plane and (*right*) along the arms for sections cut (*A*) ~135*μ*m, (*B*) ~120*μ*m, (*C*) ~60*μ*m, (*D*) ~45*μ*m and (*E*) ~15*μ*m from the ID of a 9M scaffold (see Figs. S13–S22 for X-ray data). The legend (e.g. +60*μ*m or -180*μ*m) indicates the position of the line scan relative to the symmetry plane of the section. Normalized position varies from 0 at the inner bend (IB) to 1 at outer bend (OB).

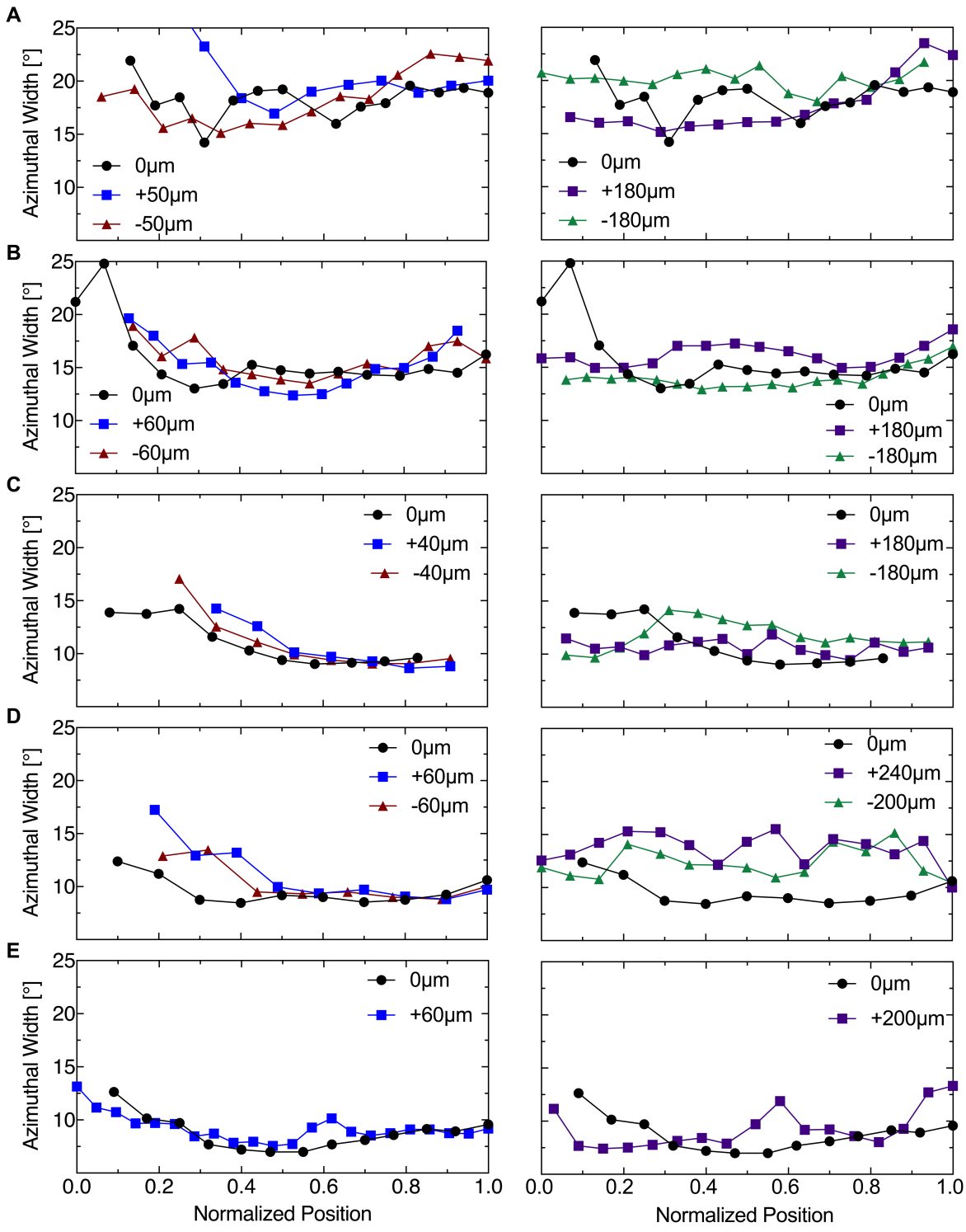

Fig. S25. The full-width at half maximum of the (110)/(200) peaks provides a measure of crystallite orientation (*left*) near the symmetry plane and (*right*) at the arms for sections cut (*A*) ~135μm, (*B*) ~120μm, (*C*) ~60μm, (D) ~45μm and (E) ~15μm from the ID of a 9M scaffold (see Figs. S13–S22 for X-ray data). The legend (e.g. +60μm or -180μm) indicates the position of the line scan relative to the symmetry plane of the section. Normalized position varies from 0 at the inner bend (IB) to 1 at outer bend (OB).

Estimating the fraction of material that resists hydrolysis in a U-crest

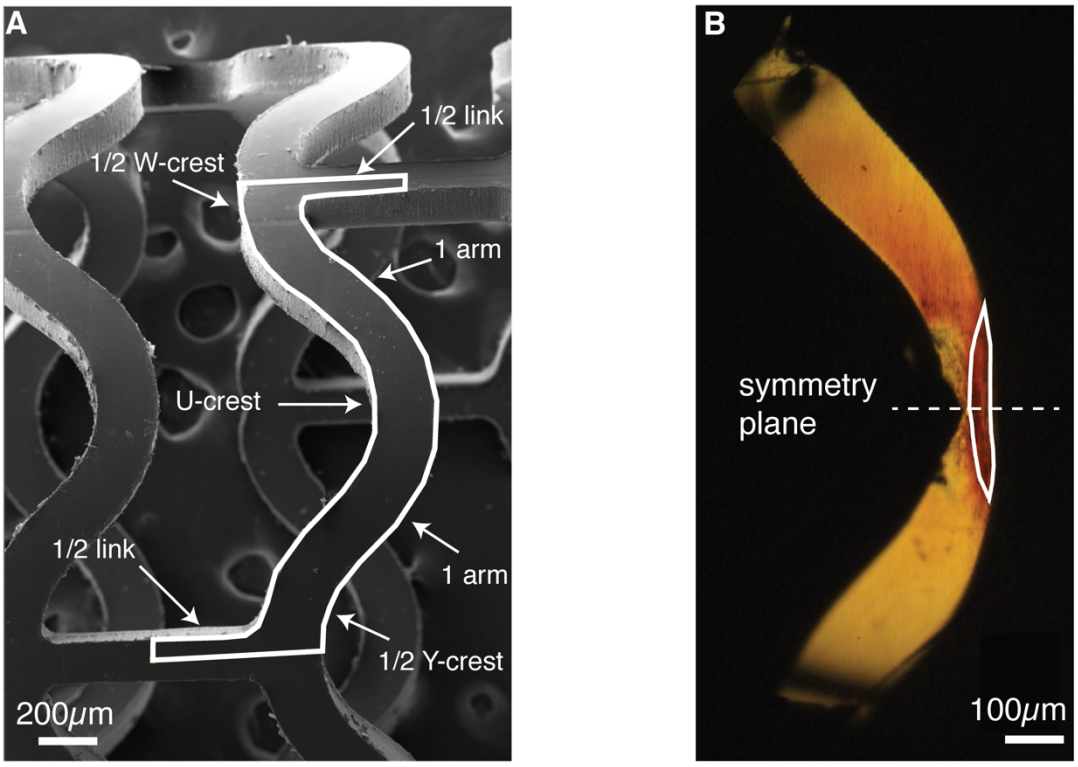

Fig. S26. (*A*) Scanning electron micrograph of an as-cut scaffold and (*B*) polarized light micrograph of a ~15μm thick section cut ~45μm from the inner diameter of a 9M scaffold (see also 45μm section in 9M, Fig. 1*D*). The highlighted portion in (*A*) identifies the basic structural unit of the struts of the scaffold. The material that resists hydrolysis in a U-crest is enclosed by the white border in (*B*).

The lattice network of struts in the clinically-approved scaffold can be constructed from a structural unit that is comprised of a U-crest, 2 arms, ½ Y-crest, ½ W-crest, ½ link connected to a Y-crest and ½ link connected to a W-crest (see highlighted portion in Fig. S26*A*). X-ray microdiffraction data acquired on U-crests indicate that the material near the outer bend (OB) of the symmetry plane (Figs. 4-5) degrades slower relative to the surrounding material (e.g. arms and links). To estimate an upper bound for the volume of material that resists hydrolysis in the scaffold, we consider material ~100μm on either side of the symmetry plane (see region outlined in Fig. 26*B*). Using the software ImageJ, we calculate the area of the region near the symmetry plane with higher than average retardation to be ~8.9 x 10^{-3} mm^2 and the area of the structural unit to be (4.6 x 10^{-1} mm^2). Over the ~140μm thickness of the OB of the deployed scaffold, we find the volume of the degradation resistant region to be approximately 1.3 x 10^{-3} mm^3, which is < 3% of the volume of the scaffold per structural unit (~6.5x$10^{-2}$$mm^3$).

Structural integrity of hydrolyzed PLLA bioresorbable vascular scaffolds

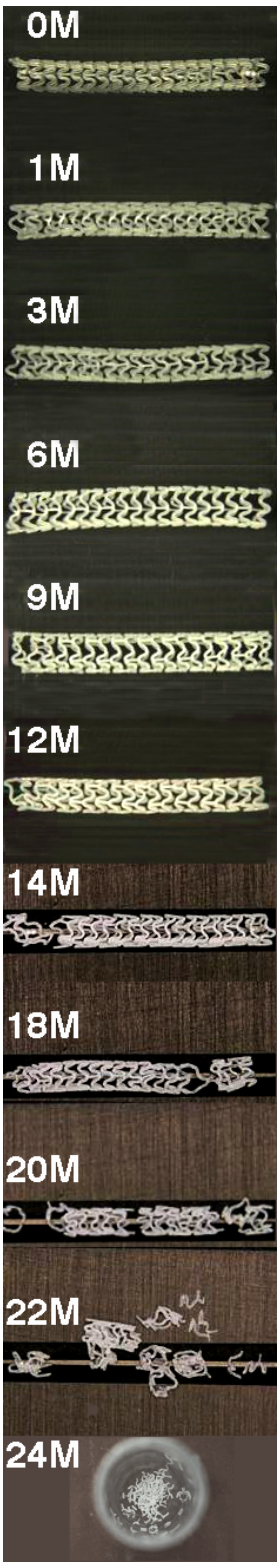

Fig. S27. Images acquired on scaffolds hydrolyzed in phosphate-buffered saline (PBS) at 37°C for 0 to 24 months. The scaffolds fall apart beyond 18 months; the rings containing U-crests remain intact while failure preferentially occurs along the links that join adjacent rings (rings and links defined in Fig. 1*A*).

X-ray diffraction Analysis

Microdiffraction data were acquired at beamline 2-ID-D (200 nm spot size, λ = 1.18 Å) of the Advanced Photon Source (APS) at the Argonne National Labs. The sample to detector distance was 80.82 mm and a Mar165 CCD detector (2048 x 2048 pixels, pixel-size = 79.13 μm) was used to acquire scattering patterns with wavevector q calibrated using a Ceria (CeO_2) standard. The 15 μm-thick microtomed sections were mounted on an aluminum post, with the r-direction of the sections parallel to the X-ray beam. The aluminum post is attached to a precision x-y stage aligned to maintain a constant sample-to-detector distance when the sample is translated in the beam. The stage was used to acquire diffraction "line scans" in 5 μm steps along the θ- and the z-direction of the sections. Two 30s acquisitions were acquired at each location on the sample; the second acquisition left a visible "burn mark" to record the exact position of each diffraction measurement. An air background was subtracted from each of the two acquisitions (described below in Figs. S28–S33), which were subsequently co-added to obtain a single diffraction pattern. Diffraction patterns were acquired at either 5 μm or 10 μm intervals along a selected line. One line-scan (usually 10 patterns) was along the symmetry plane (defined in Fig. 1*D*). Typically, four more line-scans parallel to the symmetry plane were acquired (each having 20 to 40 patterns). Thus, over 130 patterns were analyzed for most of the sections that were examined using microdiffraction. Three to five sections (at different distances from the inner diameter) were analyzed for each of the three time points (0, 9 months and 18 months of hydrolysis).

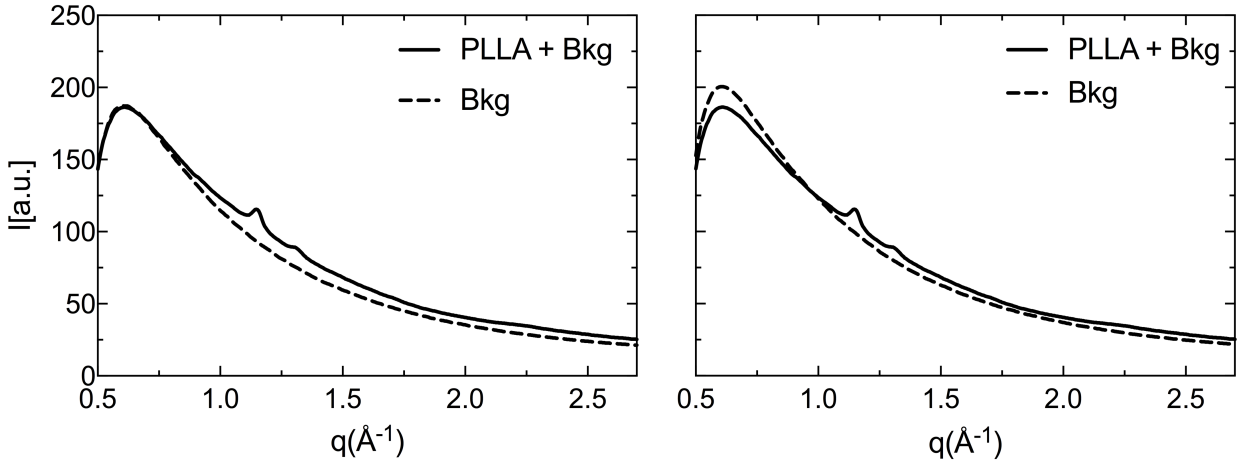

Fig. S28. Variation in background intensity, particularly at low-q (0.5-0.75 Å^{-1}), results in subtraction errors comparable to the scattered intensity from PLLA alone. Comparison between the signal from a 15 μm thick PLLA section with (*A*) background acquired immediately before (~7 mins), and (*B*) a background acquired ~5 hrs later.

The scattered intensity from a ~15 μm thick poly L-lactide (PLLA) section is barely 3% above the background (Fig. S28, *left*). Therefore, it is challenging to isolate the signal from PLLA alone when the background intensity varies in excess of 5%, particularly at low-q (0.5 to 0.55 Å^{-1}). A comparison between a PLLA I(q) plot and a background I(q) acquired 7 minutes earlier (Fig. S28, *left*) reveals little to no difference in intensity at low-q (0.5 to 0.55 Å^{-1}) and at high-q (2.7 to 2.8 Å^{-1}). However, when the same PLLA signal is compared to a background I*(q)* acquired ~5 hours later (Fig. S28, *right*), large deviations in intensity at low-q (0.5 to 1.0 Å^{-1}) are observed despite similar intensities at high-q. This suggests that fluctuations in beam intensity alone, which dominate scattering at high-q, cannot account for variations in

intensity at low-q. It appears that the background signal is changing in both intensity and shape due to variations in air temperature, humidity etc.

We probe the drift in background scatter by acquiring "air" diffraction patterns (30s exposure, no sample between the beam and the detector) before and after every line scan of microdiffraction data (Fig. S29). A set of 6 diffraction patterns, acquired within 5 hours of a microdiffraction line scan, are averaged in 2D to obtain a single "average" background pattern, which is subsequently rescaled and subtracted from each PLLA diffraction pattern (30s exposure as well) of the corresponding line scan. Here, we discuss the implementation of our subtraction approach to a section cut ~60μm from the inner diameter of a 9-month hydrolyzed scaffold (Fig. S15). The same method is applied to microdiffraction datasets acquired on other sections cut from the as-deployed (0M), 9-month hydrolyzed (9M), and 18-month hydrolyzed (18M) scaffolds using their corresponding sets of 6 background patterns.

To identify the optimal method for isolating the scattering from PLLA, we subtract the average background pattern from each of the other 6 background frames and analyze the resulting residuals. Direct subtraction of the average background results in errors comparable to 40% of the maximum intensity from a single PLLA frame (Fig. S30). Normalizing the background using the intensity at high-q (2.7 to 2.8 $Å^{-1}$), an internal standard for beam intensity, still results in subtraction errors ~20% of the intensity from PLLA alone (Fig. S31). Therefore, we test and implement a two-parameter subtraction approach that not only accounts for fluctuations in beam intensity at high-q, but also corrects for variations in air quality at low-q.

We take advantage of the fact that the scattering from a 15 μm thick PLLA section is indistinguishable from the background at low-q (0.5 to 0.55 $Å^{-1}$) and high-q (2.7 to 2.8 $Å^{-1}$) (Fig. S28, *left*). Therefore, we extract two parameters (α and β) from the PLLA frame and the average background pattern to minimize the ~5% variation in air scatter at low-q. The parameter α relates the difference in intensity (ΔI) between the sample's low-q (I_L) and high-q (I_H) intensity to that of the background, while the parameter β applies an offset to the background to match the sample's I_H. Using q and φ to represent the radial wavevector and the azimuthal angle of the sample (S) and background (B) respectively, we arrive at the following equation:

$$S(q,\varphi)_{subtracted} = S(q,\varphi) - \alpha.B(q,\varphi) - \beta \qquad [S1]$$

where $\alpha = \Delta I_S/\Delta I_B$ and $\beta = I_{H,S} - \alpha.I_{H,B}$. We apply the two-parameter subtraction method in 2D; the background is rescaled using α and β and is then subtracted pixel by pixel from each sample frame (Fig. S32). This method successfully minimizes deviations in intensity between the sample and the background at low-q (Fig. S32), and the ~ ± 1 error in subtraction has negligible impact (<5% of the maximum intensity from PLLA) on the signal from the subtracted PLLA frame (Fig. S33).

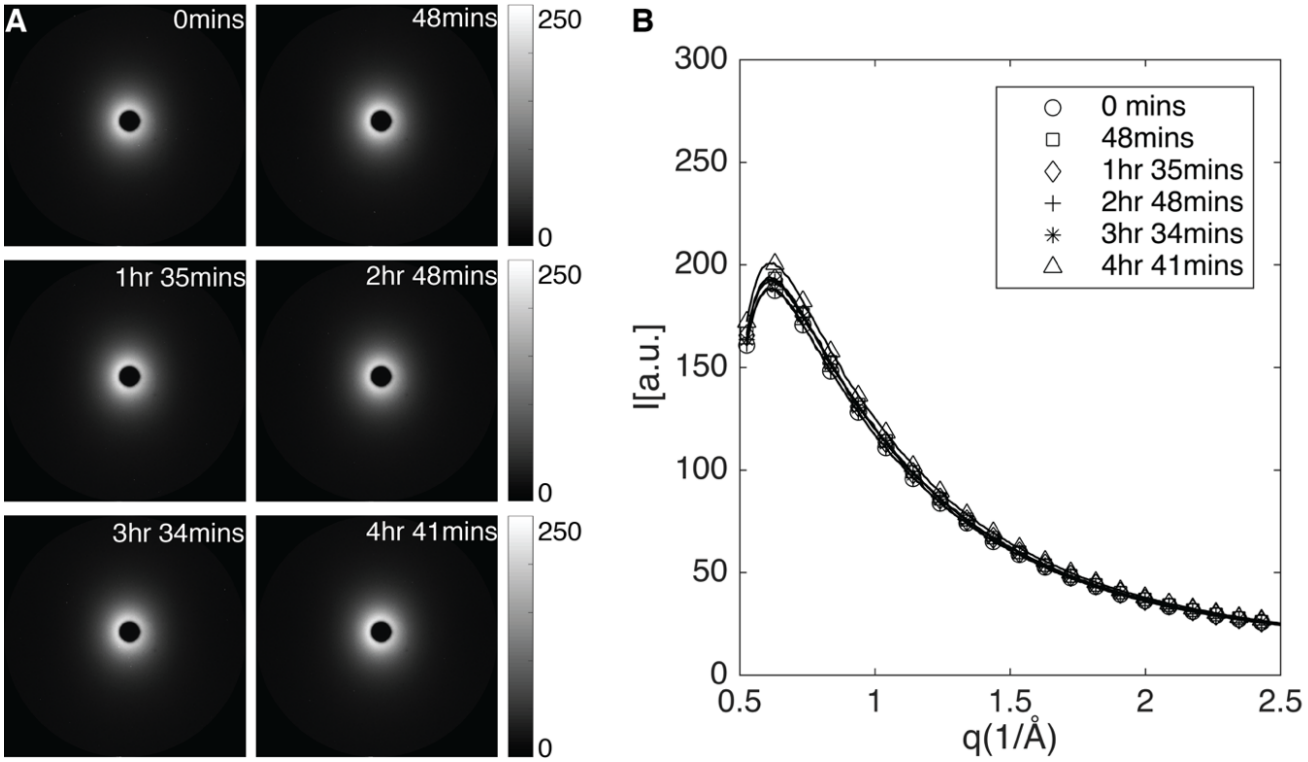

Fig. S29. Drift in background scatter over a period of ~5 hrs during data acquisition on the 9M section. Background scatter is presented as (*A*) 2D diffraction patterns and (*B*) azimuthally averaged I(*q*) plots.

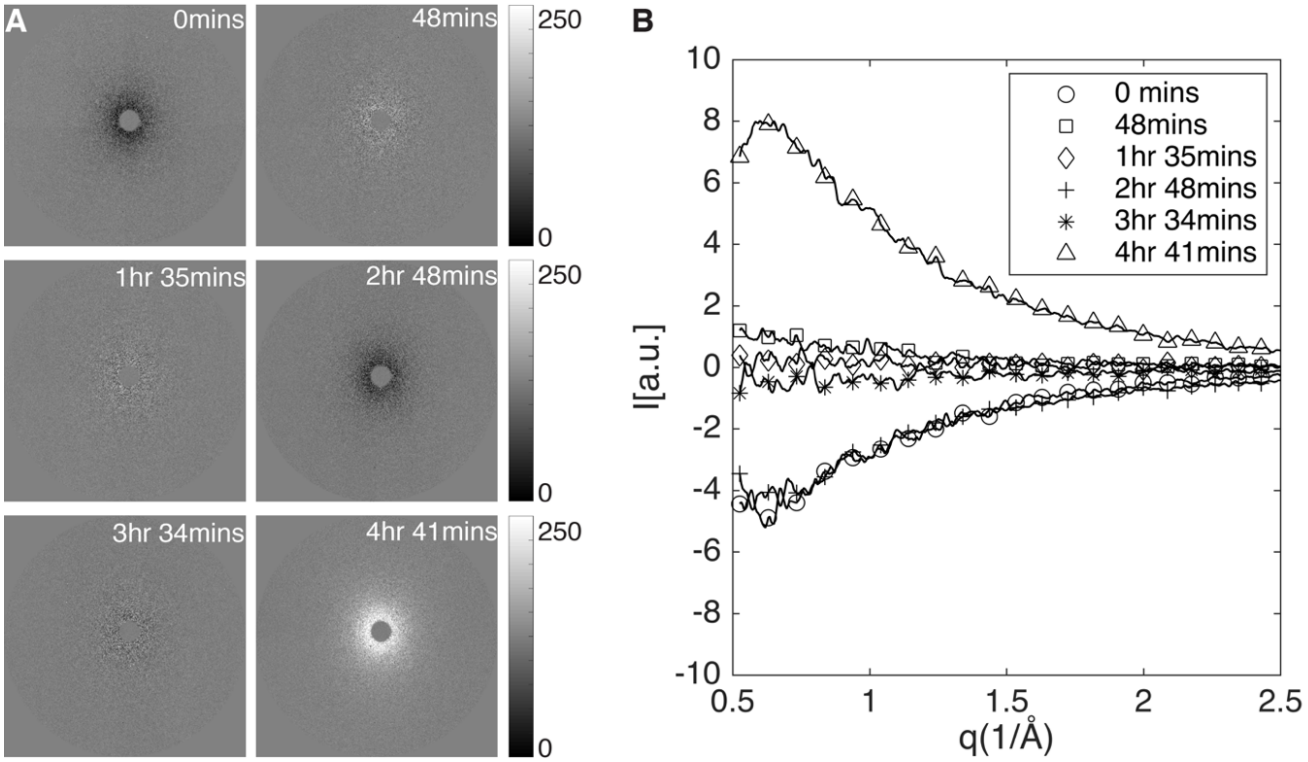

Fig. S30. Deviations in residual intensity, particularly at low-*q*, when the average background pattern is directly subtracted (no scaling) from the six background patterns presented in Figure S29. The residuals are presented as (*A*) 2D diffraction patterns and (*B*) azimuthally-averaged, I(*q*), plots.

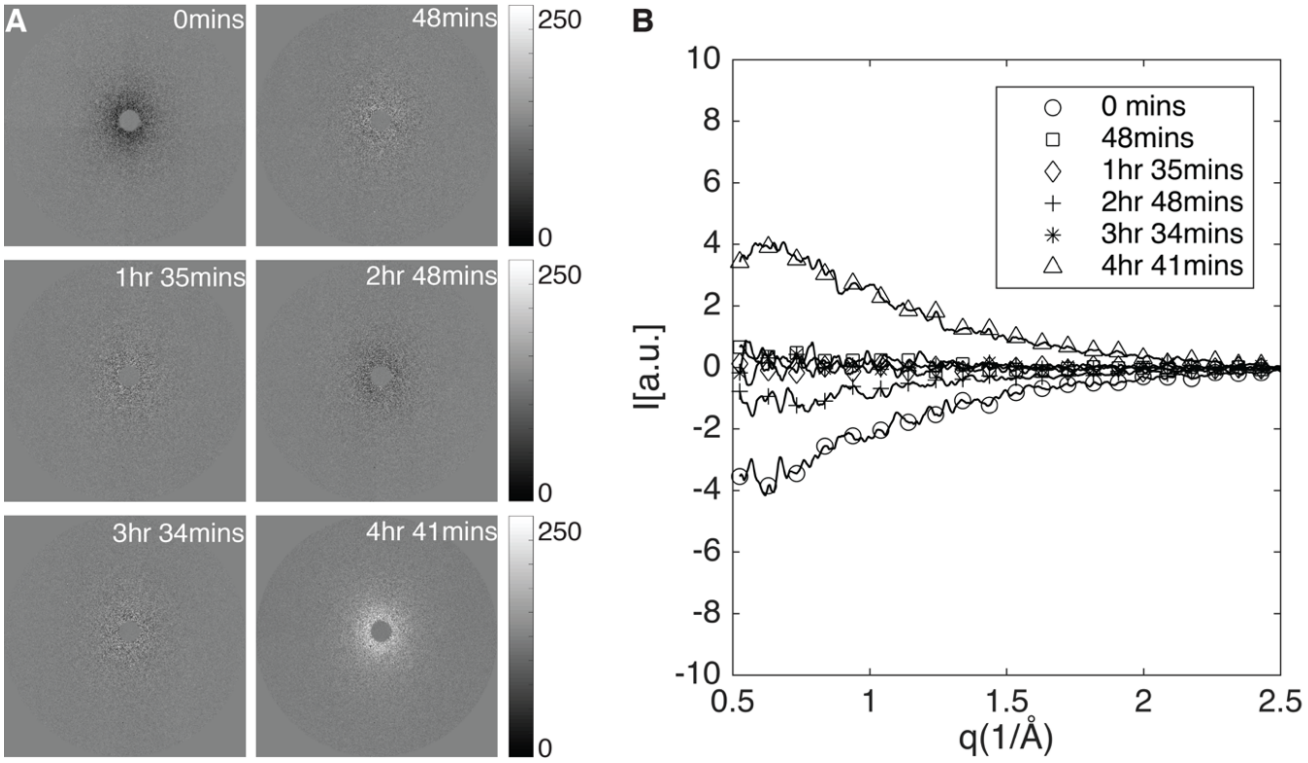

Fig. S31. Deviations in residual intensity are significant despite rescaling the average background using an internal standard to account for fluctuations in beam intensity. The residuals are presented as (A) 2D diffraction patterns and (B) azimuthally-averaged, I(*q*), plots.

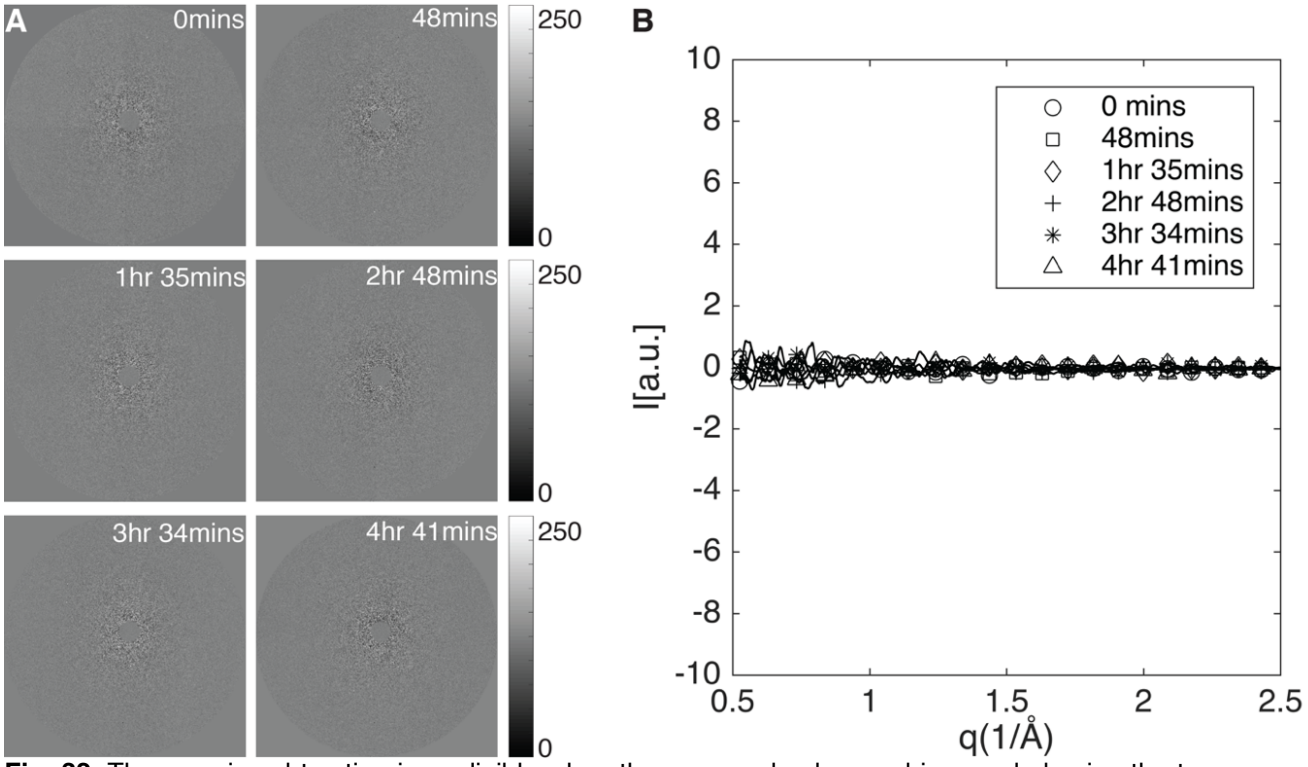

Fig. 32. The error in subtraction is negligible when the average background is rescaled using the two-parameter approach to account for fluctuations in air scatter that dominate intensity at low-*q*, and for variations in beam intensity

that dominate scattering at high-*q*. The residuals are presented as (*A*) 2D diffraction patterns and (*B*) azimuthally-averaged, I(*q*), plots.

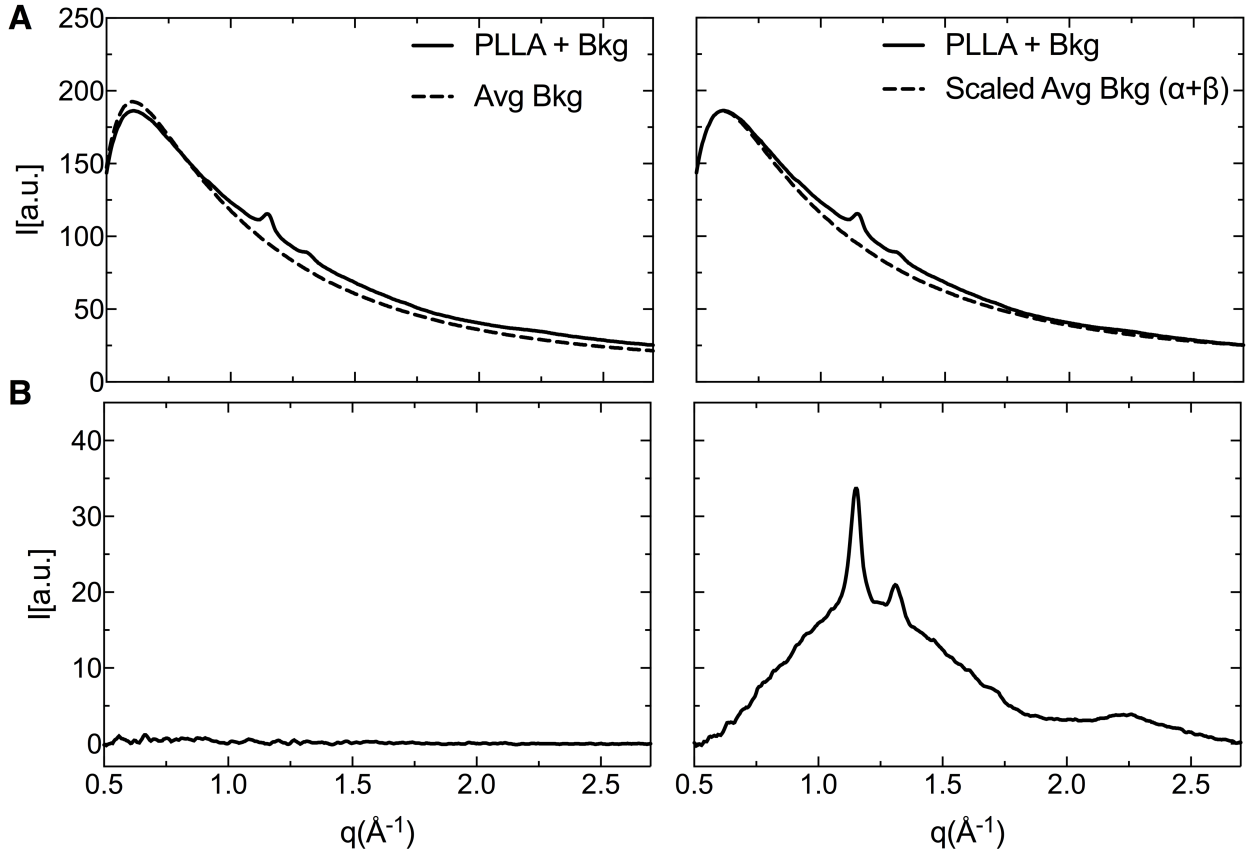

Fig. 33. The two-parameter subtraction method rescales the average background (dashed line, A, *left*) to minimize deviations in intensity between the sample (solid line, A, *left*) and the background at low-*q* (0.5-1Å^{-1}). The rescaled background (dashed line, A, *right*) is comparable to a background frame acquired immediately before the sample frame (see Fig. S28, *left*); this method introduces minimal error (B, *left*) and has negligible impact on the resulting PLLA signal (B, *right*).

References:

1. Rapoza R, Veldhof S, Oberhauser J, Hossainy (2015) Assessment of a Drug Eluting Bioresorbable Vascular Scaffold. US Patent Appl No. 14/121,435.
2. Kossuth MB, Perkins LEL, Rapoza RJ (2016) Design Principles of Bioresorbable Polymeric Scaffolds. *Interv Cardiol Clin* 5(3):349–355.
3. Li S (1999) Hydrolytic degradation characteristics of aliphatic polyesters derived from lactic and glycolic acids. *J Biomed Mater Res* 48(3):342–353.
4. Tsuji H, Mizuno A, Ikada Y (1999) Properties and Morphology of Poly (L -lactide). III . Effects of Initial Crystallinity on Long-Term In Vitro Hydrolysis of High Molecular Weight Poly (L -lactide) Film in Phosphate-Buffered Solution. *J Appl Polym Sci*:1452–1464.
5. Fischer EW, Sterzel HJ, Wegner G (1973) Investigation of the structure of solution grown crystals of lactide copolyers by means of chemical reactions. *Kolloid-Z.uZ Polym* 251(11):980–990.
6. Ailianou A, Ramachandran K, Kossuth MB, Oberhauser JP, Kornfield JA (2016) Multiplicity of morphologies in poly (l-lactide) bioresorbable vascular scaffolds. *Proc Natl Acad Sci* 113(42):11670–11675.
7. Glauser T, et al. (2015) Controlling Crystalline Morphology of a Bioabsorbable Stent. US Patent Appl No. 13/734,879.